Global high-resolution simulations of CO_2 and CH_4 using a NIES transport model to produce a priori concentrations for use in satellite data retrievals

T. Saeki[1], R. Saito[2], D. Belikov[1], and S. Maksyutov[1]

[1] {Center for Global Environmental Research, National Institute for Environmental Studies, Tsukuba, 305-8506, Japan}

[2] {Research Institute for Global Change, JAMSTEC, Yokohama, 236-0001, Japan}

Correspondence to: T. Saeki (saeki.tazu@nies.go.jp)

Keywords: Carbon dioxide (CO_2), Methane (CH_4), global tracer transport model, high-resolution meteorological data, satellite retrieval

Abstract

The Greenhouse gases Observing SATellite (GOSAT) measures column-averaged dry air mole fractions of carbon dioxide and methane (XCO_2 and XCH_4, respectively). Since the launch of GOSAT, model-simulated three-dimensional concentrations from a National Institute for Environmental Studies offline tracer Transport Model (NIES TM) have been used as a priori concentration data for operational near real-time retrievals of XCO_2 and XCH_4 from GOSAT short-wavelength infrared spectra at NIES. Although a choice of an a-priori profile makes minor effect on retrieved XCO_2 or XCH_4, a realistic simulation with minimal deviation from observed data is desirable. In this paper we describe the newly developed version of NIES TM that has been adapted to provide global and near real-time concentrations of CO_2 and CH_4 using a high-resolution meteorological dataset, the Grid Point Value (GPV) prepared by the Japan Meteorological Agency. The spatial resolution of the NIES TM is set to 0.5° × 0.5° in the horizontal in order to utilize GPV data, which have a resolution of 0.5° × 0.5°, 21 pressure levels, and a time interval of 3 hours. GPV data are provided to the GOSAT processing system with a delay of several hours, and the near real-time model simulation produces a priori concentrations driven by diurnally varying meteorology. A priori variance–covariance matrices of CO_2 and CH_4 are also derived from the simulation outputs and observation-based reference data for each month of the year at a resolution of 0.5° × 0.5° and 21 pressure levels. Model performance is assessed by comparing simulation results with the GLOBALVIEW dataset and other observational data. The overall root-mean-square differences between model predictions and GLOBALVIEW analysis are estimated to be 1.45 ppm and 12.52 ppb for CO_2 and CH_4, respectively, and the seasonal correlation coefficients are 0.87 for CO_2 and 0.53 for CH_4. The model showed good performance particularly at oceanic and free tropospheric sites. The high-resolution model also performs well in reproducing both the observed synoptic variations at some sites, and stratospheric profiles over Japan. These results give us confidence that the performance of our GPV-forced high-resolution NIES TM is adequate for use in satellite retrievals.

1 Introduction

Global atmospheric transport models provide an effective means of quantifying the global cycle of long-lived atmospheric trace gases such as carbon dioxide (CO_2) and methane (CH_4). There is an increasing demand for high-resolution models that simulate global tracer transport over synoptic and sub-daily timescales to reproduce observed variations more accurately. For example, the Atmospheric Tracer Transport Model Intercomparison Project (TransCom) has initiated simulations of hourly and synoptic CO_2 concentration (Law et al., 2008; Patra et al., 2008), which will complement and make use of state-of-the-art measurements of greenhouse gases. In this TransCom continuous experiments, 25 transport models participated with two running at 0.5° × 0.5° resolution and the others running at 1° × 1° to 3.8° × 5.0° resolutions. Patra et al. (2008) concluded that increasing model horizontal resolution clearly improved the synoptic-scale variations in simulated CO_2. Maksyutov et al. (2008) compared model CO_2 results at horizontal resolutions of 2.0°, 1.0°, 0.5°, and 0.25° with continuous observations at a tower site in Japan and showed that increasing the model's horizontal resolution greatly improved the match with observations. However most model simulations of these greenhouse gases are still carried out at horizontal resolutions of 1° × 1° ~ 3.75°× 2.5° (e.g. Allen et al., 2012; Saito et al., 2011; Patra et al., 2011).

Another demand for the high-resolution models stems from a new approach in which model-predicted CO_2 and CH_4 concentrations are used to give a priori concentrations for satellite spectroscopic data retrieval algorithms (e.g. Saitoh et al., 2009; Yoshida et al., 2011; O'Dell et al., 2012). Satellite observations cover most of the globe in several days to a few weeks, and retrievals based on satellite spectra require a priori concentrations of targeted gases. Global transport models can provide simulated a priori concentration profiles of those greenhouse gases in order to obtain optimal retrieval solutions and to physically interpret satellite-derived data. Instantaneous fields of view of satellite instruments are of the order of 10–100 km; e.g., 30 × 120 km^2 for the SCanning Imaging Absorption spectroMeter for Atmospheric CHartographY (SCIAMACHY) (Buchwitz et al., 2005), and a nadir circular footprint of about 10.5 km diameter for the Greenhouse gases Observing SATellite (GOSAT) (Yoshida et al., 2011). For GOSAT, the retrieval precisions are estimated to be

smaller than 3.5 ppm and 15 ppb for column-averaged dry air mole fractions of both carbon dioxide and methane (XCO_2 and XCH_4), respectively (Yoshida et al., 2011). Furthermore, future satellites that observe greenhouse gases target higher precision with less bias. For example, the Orbiting Carbon Observatory-2 (OCO-2) is designed to retrieve XCO_2 theoretically with 1–2 ppm (0.3–0.5%) precision for single-soundings with a small field of view with an area of 3 km^2 in nadir (Boesch et al., 2011). Therefore, much effort is currently being devoted to the development of global high-resolution transport models with less model error that meet the demands from satellite observations of greenhouse gases. For various applications of the retrieved data such as observations of strong CO_2 emissions by forest fire or volcano eruptions, users desire a near real-time data processing. To serve those needs, an operational retrieval in GOSAT data processing system is conducted at near real-ime.

GOSAT is the first satellite to measure global distributions of XCO_2 and XCH_4 (Kuze et al., 2009; Yokota et al., 2009; Yoshida et al., 2011). At the National Institute for Environmental Studies (NIES), XCO_2 and XCH_4 are retrieved from the short-wavelength infrared (SWIR) spectra obtained by the Thermal And Near infrared Sensor for carbon Observation-Fourier Transform Spectrometer (TANSO-FTS) on board GOSAT. An optimal estimation method is used to retrieve XCO_2 and XCH_4 which minimizes the cost function

$$J(\boldsymbol{x}) = [\boldsymbol{y} - \mathrm{F}(\boldsymbol{x})]^{\mathrm{T}} \mathbf{S}_{\varepsilon}^{-1} [\boldsymbol{y} - \mathrm{F}(\boldsymbol{x})] + [\boldsymbol{x} - \boldsymbol{x}_a]^{\mathrm{T}} \mathbf{S}_a^{-1} [\boldsymbol{x} - \boldsymbol{x}_a] \quad (1)$$

where $\boldsymbol{x}$ is the state vector to be retrieved, $\boldsymbol{y}$ is the vector containing the observed spectrum, $F(\boldsymbol{x})$ is the forward model that relates the state vector to the observed spectrum, $\mathbf{S}_{\varepsilon}$ is the error covariance matrix of the observed spectrum, $\boldsymbol{x}_a$ is the a priori state of $\boldsymbol{x}$, and $\mathbf{S}_a$ is the a priori variance–covariance matrix (VCM) (Yokota et al., 2009; Yoshida et al., 2011). A priori state $\boldsymbol{x}_a$ includes a priori concentration profiles of CO_2 and CH_4. The retrieved XCO_2 and XCH_4 at NIES are available after April 2009 at GOSAT User Interface Gateway (GUIG; http://data.gosat.nies.go.jp/).

As a priori concentrations for NIES XCO_2 and XCH_4 retrievals, we use simulated data from a NIES atmospheric tracer transport model (hereafter NIES TM) (Japan Aerospace Exploration Agency, National Institute for Environmental Studies, and Ministry of the Environment, 2011 (hereafter

JAXA/NIES/MoE, 2011); Yoshida et al., 2011). The a priori VCMs, $\mathbf{S}_a$, for CO_2 and CH_4 are derived from simulated NIES TM data and some reference data (Eguchi et al., 2010). The chose of a priori concentrations for satellite data retrievals is optional, and various a priori concentrations have been used to retrieve XCO_2 and XCH_4 from GOSAT SWIR spectra; e.g, constant a priori concentrations (Oshchepkov et al., 2011), monthly zonal means in 10° latitude bands for land and ocean from a forward model run (O'Dell et al., 2012), or model-simulated concentrations for the year 2007, 2008 (Butz et al. 2011) or 2009 that was extrapolated to 2010 (Schepers et al., 2012). However, as seen in Eq. (1), when the diagonal elements of $\mathbf{S}_a$ have small values, the a priori profiles largely constrain the retrieved results (e.g. Saitoh et al., 2009; Yoshida et al., 2011). We thus aim to reduce errors in a priori CO_2 and CH_4 concentrations for use in the NIES retrieval algorithm by using NIES TM at the relatively high horizontal resolution of 0.5° × 0.5°.

Distinctive feature of the NIES a priori concentrations is that they are created by NIES TM driven by a near real-time high-resolution meteorological dataset at a horizontal resolution of 0.5° × 0.5° and 21 pressure levels. As a result, real-time SWIR retrieval processing is made available to create XCO_2 and XCH_4 products at every observed day by using a priori concentrations that reflect daily meteorological variations at the observed days. Use of high-resolution meteorological data would be expected to allow smaller-scale phenomena to be represented in the model.

In this paper, we describe a newly developed high-resolution NIES TM designed to provide near real-time global three-dimensional concentration fields that reflect daily meteorological conditions for satellite retrieval algorithms, which is currently implemented in the GOSAT Level 2 retrieval system to derive XCO_2 and XCH_4 at NIES (Sect. 2). In Sect. 3, the simulated CO_2 and CH_4 concentrations are compared with an analysis of GLOBALVIEW-CO_2 (2009) and GLOBALVIEW-CH_4 (2009) data products (hereafter GV-CO_2, GV-CH_4) and other observations to evaluate the model performance and investigate potential biases arising from the model simulation. Our conclusions follow in Sect. 4.

2 NIES transport model and numerical experiments

A NIES off-line global transport model (Maksyutov et al., 2008) has been used to simulate seasonal and spatial distributions of long-lived atmospheric constituents in the lower and mid-troposphere. The advection scheme of the model was semi-Lagrangian, and a mass fixer was adopted to conserve total mass of tracers in the model for long-term simulation. The vertical mixing in the model was represented by cumulus convection and turbulent diffusion with explicitly parameterized Planetary Boundary Layer (PBL) physical processes. The details of the mass fixer, cumulus convection, and turbulent diffusion are described in Appendix A.1 – A.3.

The earlier version of the NIES transport model (denoted NIES-99) was developed to simulate the seasonal cycles of long-lived tracer species at a relatively coarse horizontal resolution (2.5°–5.0° longitude–latitude), and to perform source–sink inversions of atmospheric CO_2 (e.g., Gurney et al., 2002, 2004; Patra et al., 2002, 2003, 2005a). Improvements to NIES-99 led to a recent development of the model (NIES-05), which has a higher horizontal resolution (tested on 2° × 2° to 0.25° × 0.25° in Maksyutov et al., 2008). NIES-05 was driven by the ECMWF 3-hourly PBL height data and the vertical resolution was enhanced to 47 levels (Appendix A.4) for better resolution of the mixing processes in the boundary layer. For more details of NIES TM, see Maksyutov et al. (2008). NIES-05 was able to simulate observed diurnal-synoptic scale variability of tracers of interest, and participated in the TransCom hourly CO_2 experiment (Law et al., 2008; Patra et al., 2008). The original version of NIES-05 used meteorology datasets from NCEP final analyses (http://dss.ucar.edu/datasets/ds083.2/).

We have recently upgraded NIES-05 to utilize a high-resolution meteorological dataset, the Japan Meteorological Agency (JMA) Grid Point Values (GPV) product (Belikov et al., 2011). GPV/JMA data is created from JMA Global Spectral Model, which is operated for short- and medium-range forecasts covering the entire globe with TL959 resolution and 60 vertical levels from the surface to 0.1 hPa and assimilated by 4D-Var within a framework of JMA's numerical weather prediction system (http://www.jma.go.jp/jma/en/Activities/nwp.html; JMA, 2007). Original GPV data is provided at 0.5° × 0.5° horizontal resolution from the surface to 100 hPa

and 1.0˚× 1.0˚ above 100 hPa to 10hPa (http://www.jmbsc.or.jp/hp/online/f-online0a.html). For use in GOSAT project, GPV data is specially extended at resolution of 0.5˚ × 0.5˚ up to 10 hPa. Since November 2007, the extended GPV has been supplied for the GOSAT Data Handling Facility (DHF; JAXA/NIES/MoE, 2011) at NIES in near-real time (delay of several hours). The spatial resolution of the GOSAT version of the GPV dataset is 0.5° × 0.5° on 21 pressure levels (from 1000 to 10 hPa) and the time resolution is 3 hours. We used both GPV objective analysis and forecasts. The GPV data and the ECMWF 3-hourly PBL height data in GRIB2 format are automatically converted to direct access binary for NIES TM input on DHF everyday. Data size is about 1.1 G bytes per one model day.

We employed the NIES-05 model driven by GPV data to simulate atmospheric CO_2 and CH_4 concentrations for use as a priori concentrations for GOSAT SWIR Level 2 processing at NIES. The horizontal resolution was 0.5° with 47 sigma vertical levels from the surface to 0.02 sigma, and simulated CO_2 and CH_4 concentrations were calculated for every observed day. The 21-level GPV data is interpolated to the model sigma levels just after reading GPV data every time step, and the model results are outputted every 3-hour time after interpolating 21 pressure levels. Flux climatologies were prepared because no real-time fluxes were available. The climatological CO_2 flux dataset was that prepared for the TransCom model inter-comparison studies (Gurney et al., 2004), which consisted of four components: (1) annual constant fossil fuel emissions with a spatial resolution of 0.5° × 0.5° (Brenkert, 1998); (2) hourly terrestrial biosphere flux obtained using the Carnegie-Ames-Stanford-Approach (CASA) model (Randerson et al., 1997); (3) monthly varying ocean flux (Takahashi et al., 2002); and (4) monthly flux corrections obtained using the cyclostationary inversion approach (Gurney et al., 2004) with NIES-99. The annual total net flux of CO_2 to the atmosphere is 4.32 GtC. For CH_4, we used the monthly varying flux for 2000 (575 Tg/yr), as obtained from Patra et al. (2009). This CH_4 flux is based on the Emission Database for Global Atmospheric Research (EDGAR) version 32FT2000 (Olivier and Berdowski, 2001) for anthropogenic CH_4, and on GISS emissions (Fung et al., 1991) for natural CH_4. The chemical destruction of CH_4 by OH radicals was calculated based on climatological monthly mean OH radical concentrations (Spivakovsky et al.,

2000) and a temperature-dependent rate constant. All these flux datasets were prepared at a spatial resolution of 1° × 1°, except for the CO_2 fossil fuel emission.

Stratospheric CO_2 and CH_4 variations are poorly understood due to a lack of precise observations over the globe. In addition, it is difficult to reproduce accurately transport and chemical processes in the stratosphere in NIES TM. This is a common problem in many transport models, where the model age of air in the stratosphere tends to be younger than that observed (Saito et al., 2011, and references therein). To reduce model biases in the stratosphere, the model stratospheric concentrations above the diagnosed tropopause are nudged towards the zonal-mean climatological concentrations based on observations. The tropopause in the model is determined from the gradient of potential temperature versus geopotential height at every model grid box at every time step. Zonal-mean climatologies for CO_2 and CH_4 were prepared at 2.5° resolution for every month. CO_2 monthly climatological concentrations in the stratosphere were constructed using the Gap-filled Ensemble Climatology Mean (GECM; Saito et al., 2011). GECM is a three-dimensional daily CO_2 concentration generated by combining information from in situ measurements and multi-model means, carried out in the framework of the TransCom satellite experiment in which six models participated. The mean age of air in the GECM stratosphere has been corrected using in situ profiles of SF_6. The latest version of GECM was used here with further corrections in the stratosphere; i.e., the vertical gradient in GECM CO_2 concentration at northern mid-latitudes from 30 hPa to 10 hPa was corrected to match CO_2 observations (Aoki et al., 2003; Engel et al., 2009). The climatological stratospheric CO_2 values were prepared from 2007 to 2015 with interannual variations for CO_2. Extension of CO_2 climatology has been done by using average trend plus average seasonal cycle obtained from fitting GV-CO_2 data (Masarie and Tans, 1995) and by using stratospheric age of air (Saito et al., 2011). This stratospheric corrections was about –0.5 ppm for XCO_2 in the northern mid latitudes.

For CH_4, monthly climatological values in the stratosphere were derived from satellite measurements by the Halogen Occultation Experiment (HALOE) (Russell et al., 1993), averaged over the period 1994–2005 to exclude the period of the Pinatubo eruption in 1991. HALOE provides a long time series of

data, from October 1991 to November 2005 (Russell et al., 1993). Park et al. (1996) validated HALOE CH_4 data against the following correlative data from space-borne infrared spectroscopy: the Atmospheric Trace Molecule Spectroscopy Experiment; the MARK IV balloon-borne Fourier transform spectrometer; rocket-based cryogenic whole air sampler, balloon-borne laser in situ sensor; and the Kernforschungsanlage cryogenic whole air sampler. They concluded that the total error for the 0.3 to 50 hPa region was less than 15% and the precision was better than 7%. Thus, we consider the HALOE CH_4 data set would be suitable for making climatological stratospheric CH_4 distributions. No clear trend had been seen in HALOE time series; thus, we repeatedly used the same monthly concentrations every year. This stratospheric corrections was about –50 ppb for XCH_4 in the northern mid latitudes.

The model was initialized with zonal-mean concentration fields on 1 January 2007 derived from GECM for CO_2 and GV-CH_4 (GLOBALVIEW-CH_4, 2009) for CH_4. As GPV data are only available after November 2007, the model for 2007 was forced with GPV 2008 data. CH_4 emissions were scaled to reproduce the 2007–2008 CH_4 trend at the South Pole (SPO) observed by the National Oceanic and Atmospheric Administration/Earth System Research Laboratory (NOAA/ESRL) in the WMO World Data Centre for Greenhouse Gases (WDCGG) database (http://ds.data.jma.go.jp/gmd/wdcgg/wdcgg.html). After 2 years of spin-up with 2008 meteorological data, simulated concentrations at the model's southernmost grid box at 1 February 2009 were readjusted by offsets to the observed NOAA/ESRL CO_2 and CH_4 values at the South Pole from the WDCGG dataset. The model was then handed over for operational processing on the GOSAT DHF after February 2009. The JMA provides the GOSAT DHF with GPV data within a day and the near real-time model simulation has been performed for every observation day. The simulated CO_2 and CH_4 concentrations at 21 pressure levels have been provided as a priori concentrations to the GOSAT Level 2 data processing to retrieve XCO_2 and XCH_4 from SWIR spectra at NIES. Model integration time for one day for two tracers (CO_2 and CH_4) is about 530 seconds by wall-clock time on a single CPU in the NIES Supercomputer System (NEC SX-8R/128M16).

To produce a priori VCMs of CO_2 and CH_4 in Eq. (1), we used the simulated concentrations for the year 2008, GV-CO_2, GV-CH_4 and observational da-

ta. The details of the procedure to produce VCMs were described in Eguchi et al. (2010). In brief, the VCM was defined as the sum of the bias and noise components, where the bias was obtained from the difference in seasonal cycle between simulated results of NIES TM and GV data, and the noise components consist of synoptic and interannual variations. The synoptic term was calculated from NIES TM results and interannual variations are derived from GV datasets over a few decades. The VCMs of CO_2 and CH_4 were prepared at each grid box of 0.5° × 0.5°, on 21 pressure levels over the globe for each month. In this study we modified the stratospheric part of the previous version of VCMs to obtain more realistic values; i.e., stratospheric CO_2 and CH_4 seasonal biases were set to the standard deviations of balloon-borne observations over Japan (Aoki et al., 2003; T. Nakazawa and S. Aoki, unpublished data, 2009), and HALOE, respectively. The resulting variances (diagonal elements) in the stratosphere were about 2–3 ppm^2 for CO_2 and about 500–10,000 ppb^2 for CH_4. Figure 1 shows VCMs for CO_2 and CH_4 over Sanriku, Japan (141.8°E, 39.2°E) in August. The values of diagonal elements are large near the surface and decrease with height. They show positive correlations, particularly near the surface. The off-diagonal elements are positive around the diagonal elements, while there are negative correlations between some pressure levels. Correlations in the stratosphere (200-10 hPa) are close to zero, indicates a weak correlation between tropospheric and stratospheric time series.

3 Results and discussion

In the following subsections, we evaluate the model performance against the analyzed data from GV-CO_2 and GV-CH_4, and other observations. Annual mean and monthly biases of the simulated CO_2 and CH_4 are examined in Sects. 3.1 and 3.2, respectively. Synoptic variations that include annual trends are validated against some sites in the WDCGG dataset in Sect. 3.3. Balloon-borne observations in the stratosphere are used to validate the simulated vertical profiles in Sect. 3.4. Finally, the simulated surface CO_2 and CH_4 concentrations and their column-averaged dry air mole fractions are presented in Sect. 3.5. For all the comparisons, the nearest horizontal and vertical model grid box to the observation location is selected. For comparison, simulations with lower horizontal resolution of 2.0° were performed with the same simulation set-up.

3.1 Comparison with observations: Annual-mean biases

Annual means of simulated CO_2 and CH_4 concentrations are compared with those from GV analysis (GLOBALVIEW-CO_2, 2009; GLOBALVIEW-CH_4, 2009) for the year 2008 at 155 (CO_2) and 123 (CH_4) GV sites (Fig. 2) because no GV-CH_4 dataset is available for the years 2009 and 2010. Active sites in 2008 were used for comparisons. Annual mean biases of the simulated concentrations against GV analysis are shown in Table 1 and Fig. 3. Simulated results averaged over 13:00–16:00 LT were used for the comparison. In general, the annual mean model biases (difference between simulations and GV analysis) are found to be less than ~1 ppm for CO_2 and ~10 ppb for CH_4 at oceanic and Southern Hemisphere sites. The model also reproduces the GV pole-to-pole gradients very well for both CO_2 and CH_4. In general, CO_2 might be expected to reproduce the GV data better than CH_4 because the CO_2 climatological flux data set includes flux correction by an inversion while CH_4 does not.

For CO_2, the average annual mean bias and its standard deviation are –0.25 ± 1.47 ppm and RMSD of 1.45 ppm (Table 1), which shows good agreement with less than 1 % between the model prediction and the GV data at most of the sites. Some inland or near-continental sites show significant positive biases (e.g., LJO, La Jolla, California, 32.90°N, 117.30°W, 10 m a.s.l; HUN, Hegyhatsal, Hungary, 46.95°N, 16.65°E, 248 m a.s.l.) or negative biases (BSC, Black Sea, Constanta, Romania, 44.17°N, 28.69°E, 3 m a.s.l). LJO is located on the west coast of California and the GV dataset shows a clear seasonal cycle with small synoptic variations, which only involve differing oceanic air masses. However a large point source with CO_2 15 ppm higher than the surroundings appears on the model grid close to LJO, and it is clear that in the model LJO is affected by plumes from this point source. This may explain the large model–observation mismatch at LJO. This might be caused by marine-only selection of LJO observations, climatological CO_2 fluxes and the high variability observed near source regions, which is not expected to be captured by global scale transport models. Even with the NIES TM 0.5° grids, such sub-grid scale dynamics could not be represented in the model. The BSC site is located in a coastal region of the Black Sea. Pérez-Landa et al. (2007a, b) studied the effect of regional and local meteorological conditions on CO_2 transport in the coastal

area of Valencia, Spain, and concluded that coastal circulation and strong local flux gradients introduced large biases against observations in a model. When a digital filter is applied to the BSC record in the GV data, large irregular seasonal variations of about –5 to +5 ppm are found, against regular seasonal peak-to-peak amplitudes of 14.8 ppm. BSC appears to be affected by local-scale circulation and/or local fluxes, and this may explain the failure of the model to reproduce BSC variations, as is the case also with HUN. The HUN site, a tall tower site, has the largest model–observation mismatch in the TransCom 3 seasonal experiment (Gurney et al., 2004). The model tends to overestimate GV data at some of the tower sites (e.g., AMT012 and AMT107, Argyle, Maine, United States, 45.03˚N, 77.53˚W, 50 m a.s.l.), mainly because of a failure to reproduce the large seasonal amplitudes and interannual variations, due to their location in areas affected by biogenic CO_2, such as forest or inland plain, where it is difficult to fully represent by the hourly climatological biogenic flux used in the model.

The simulated CH_4 mostly agree well with the GV data, with an average annual mean bias and standard deviation of –0.31 ± 12.57 ppb and RMSD of 12.52 ppb (Table 1). Significant positive or negative biases are found in Eurasia (TAP, Tae-ahn Peninsula, Republic of Korea, 36.73˚N, 126.13˚E, 20 m a.s.l;), and North America (BNE010, Beaver Crossing, Nebraska, airborne observation, 40.80˚N, 97.18˚W, 0-2000 m) with maximum 76 ppb and minimum –49 ppb. TAP, on the western edge of Korea, is influenced by seasonally varying wind direction, and local and remote CH_4 sources such as wetland (Dlugokencky et al., 1993), and this causes large interannual and seasonal variations, which the model finds difficult to reproduce. Located in the American Prairie, CH_4 at BNE010 exhibits scattered and large interannual variations and seasonal cycles, which is also difficult to reproduce by the model.

3.2 Comparison with observations: Monthly biases

To assess the ability of the model to reproduce seasonal variations, the simulated monthly mean concentrations of CO_2 and CH_4 for the year 2008 were compared with the analyzed seasonal cycles at GV sites (Fig. 4). Analyzed seasonal cycles at GV sites were taken from “seas” files stored in the dataset. The simulated results were detrended and monthly means of 13:00–16:00 LT con-

centrations used for the comparison.

The characteristics of the observed seasonal variability at oceanic sites and free troposphere sites (above 3000 m altitude) are generally reproduced fairly well by the model for both CO_2 and CH_4, but relatively large biases are found at tower sites and some of the land sites. Standard deviations over all GV sites are 1.47 ppm for CO_2 and 12.57 ppb for CH_4. Large seasonal biases over 10 ppm in CO_2 are seen at tower sites in mid-northern latitudes such as AMT and LEF (Park Falls, Wisconsin, United States, 45.95°N, 90.27°W, 472 m a.s.l.); both sites provide continuous measurements and are located near forested areas on the eastern coast of the United States. Seasonal biases at AMT and ITN show that the model seasonal amplitudes are smaller than those in the GV analysis; i.e., the model overestimates the observed summer minima in July and August and underestimates winter maxima. At continental sites with quasi-continuous measurements such as the towers, both the regional-local transport and daily flux variability, including temporal resolution of the biospheric fluxes, are found to be important in simulating such high-frequency CO_2 behavior (Geels et al., 2004, 2007; Patra et al., 2008; Wang et al., 2007). Patra et al. (2008) also found that at lower levels some models overestimated the magnitudes of synoptic variations at high-frequency observational sites at tall towers such as LEF. These small-scale phenomena may influence model–observation mismatches at tower sites even though the comparisons are on a monthly basis. Except for such tower sites and inland sites, the model succeeds in capturing the GV seasonal variations with biases smaller than 5 ppm at most sites and for most months.

For CH_4, the monthly model biases fall within about 20 ppb at oceanic and free troposphere sites (mostly airborne observational points). In particular, there appear to be no significant monthly model biases in the Southern Hemisphere. The seasonal biases for oceanic sites increase as move north-poleward with a maximum bias about 30 ppb. At continental sites such as TAP (Korea) and BSC (Romania), the agreement was poorer, mainly due to the influences of strong sources located near the sites and extreme climate conditions such as a strong inversion layer in a cold winter.

Statistics of monthly CO_2 and CH_4 biases against the GV analysis for the year 2008 are shown in Table 1 and Fig. 5. The overall correlation coefficients

between the observed and modeled seasonal patterns at the GV sites are 0.87 for CO_2 and 0.53 for CH_4, which shows a high degree of consistency between the model and the GV analyses. High correlations are found particularly at oceanic sites: correlation coefficients are 0.97 and 0.70 for CO_2 and CH_4, respectively. Total model–observation differences (CRMSD in Table 1) are 0.50 and 1.08 for CO_2 and CH_4, respectively, and better performance are found at oceanic sites. Generally, the model underestimates the GV CO_2 amplitudes (total RSTD 0.78) and overestimates the GV CH_4 amplitudes (total RSTD 1.20). Simulated CO_2 and CH_4 at the tower sites show relatively poorer performance, particularly for the CH_4 case with correlations of 0.65 for CO_2 and 0.025 for CH_4. Tower sites are typically located near source regions on land. The use of the climatological flux dataset might make it difficult for the model to reproduce the large variations observed at the tower sites. Model transport errors such as PBL height, vertical diffusion may affect the model's ability to reproduce the CO_2 concentration observed at tower sites. Except for the tower sites, the model shows statistically good performance at the oceanic, land, and free tropospheric sites. The performance of the higher-resolution model is not improved from the lower-resolution model, thus the simulated monthly seasonal variations are mostly limited by the climatological fluxes.

3.3 Comparison with observations: Synoptic variations

Daily averages from the simulated results and observations were compared at Mauna Loa, Hawaii (MLO; 19.5°N, 155.6°W, 3397 m a.s.l), South Pole, Antarctica (SPO; 89.98°S, 24.8°W, 2810 m a.s.l.), and Hateruma, Japan (HAT; 24.05°N, 124.8°E, 47 m a.s.l.), Cape Ochi-ishi, Japan (COI; 43.15°N, 145.50°E, 96 m a.s.l.). CO_2 and CH_4 data at MLO and SPO were provided by NOAA/ESRL in the WDCGG dataset (Dlugokencky 2012a, 2012b; Thoning 2012a, 2012b). Daily CO_2 data at HAT and COI were available from the Greenhouse Gases Trend Update (http://db.cger.nies.go.jp/g3db/ggtu/index.html) operated by the Center for Global Environmental Research (CGER), NIES. CH_4 data at HAT are hourly data (Tohjima et al., 2002, 2010; T. Tohjima, unpublished data, 2011). CH_4 observations at SPO are discrete observations and the other observations are continuous measurements. The continuous data and the 3-hourly model output were daily averaged based on local time for each site. As de-

452 scribed in Sect. 2, GPV data are only available after December 2007, so the
453 year 2008 meteorological data were used from January to November 2007 for
454 the simulation.
455 Comparisons with continuous measurements of CO_2 and CH_4 show that
456 the model was able to capture the observed synoptic and seasonal variations at
457 each monitoring station (Fig. 6). Simulated CO_2 at MLO shows good agree-
458 ment with the observed CO_2 though the model underestimates the observed
459 spring maxima in 2008 and 2010, while simulated CH_4 at MLO slightly under-
460 estimates the observed CH_4 by about 20 ppb after 2009. MLO is remote from
461 the large source regions, which are mainly on land, and transport is therefore
462 a dominant factor for CO_2 variability. Unlike CO_2, CH_4 reacts with OH radi-
463 cals during transport, which affects CH_4 variability. The interannual variabil-
464 ity of atmospheric circulation is also important for the growth rate at MLO be-
465 cause transport determines the area the airmass come from, such as boreal
466 Asia, the North Pacific, or the tropical Atlantic (Higuchi et al., 2002; Patra et
467 al., 2005b). In this mean, the model transport reproduces the overall features
468 of observed CO_2 and CH_4 at MLO, but the use of climatological fluxes in this
469 study gives some discrepancies. At SPO, another remote site away from strong
470 source regions, the observed CO_2 has very small seasonal variations. A gap in
471 the simulated CO_2 at the end of January 2009 is due to the offset correction
472 described in Sect. 2. Differences between the model and the observed small
473 variations in the first half of 2010 are slightly large at 2 ppm, which might be
474 due to climatological CO_2 fluxes and model transport error. Otherwise, the
475 simulated CO_2 trend generally matches the observed one. In spite of the OH
476 sink, the simulated CH_4 reproduces the observed CH_4 at SPO very well except
477 for the second half of 2010, where there occurs a large increase in observed
478 CH_4.
479 HAT is an island located on the East-Asian continental margin and is in-
480 fluenced by air masses transported from the Pacific Ocean in summer and
481 from the continent in winter (Tohjima et al., 2002, 2010). Larger seasonal am-
482 plitudes and larger synoptic events are therefore observed here, relative to the
483 background sites MLO and SPO. Though the CO_2 fluxes in the model are cli-
484 matological, the model can simulate the observed seasonal pattern and occa-
485 sional synoptic events such as the low concentrations in August 2008 and 2009.

High-CO_2 events in winter are difficult to represent perfectly in the model, possibly due to transport of CO_2 from continental urban areas, but the model successfully simulates observed spring maxima. CH_4 at HAT is also well reproduced by the model; i.e., the model shows a clear seasonal pattern of summer and winter air mass exchanges. The model sometimes even captures sudden summer high CH_4. Basically HAT is covered by oceanic air mass and the CH_4 fluxes in the model are climatological; thus, these high-CH_4 events are thought to be CH_4 transported from continental CH_4 source regions.

COI is located in the eastern part of Hokkaido, Japan. The monitoring station fronts onto the northwest Pacific Ocean and is influenced generally by northwesterly winds in winter and southwesterly winds in summer (Tohjima et al., 2002). Reflecting seasonal variations of seasonally-varying air mass from Japan and East Asia, CO_2 concentration at COI shows larger seasonal variation than that at HAT. The model captures overall features of CO_2 trend and seasonal variations at COI.

Table 2 lists the statistics (ratio of standard deviations, correlation coefficients, overall biases, centered pattern root-mean-square differences) between daily averaged modeled and observed CO_2 and CH_4 at the three sites. As described above, only CH_4 at SPO is discrete data and the modeled CH_4 is taken from the same date and time as the observation. The statistics suggest that the model can simulate the observed daily CO_2 and CH_4 variations fairly well with a correlation coefficient (r) > 0.8 at the three sites, except for CH_4 at MLO (r = 0.59). The calculated RSTDs are nearly 1 and overall biases are less than 1 ppm for CO_2 and 10 ppb for CH_4. CRMSDs are also below 1, indicating that the model performs reasonably well.

Figure 7 illustrates synoptic-scale variations of CO_2 and CH_4 at HAT and CO_2 at COI. Synoptic variations were deseasonalized and detrended variations which were extracted from the observed and simulated time series (Fig. 6) by using a digital filter technique (Nakazawa et al., 1997). The synoptic variation in CO_2 at HAT is larger in summer than in winter due to air mass from East Asia. CH_4 at HAT observed numerous peaks throughout the year, which reaches at about 150 ppb. CO_2 at COI has large synoptic variability in summer time. Table 3 lists statistics of the model performances of 0.5° and 2.0° simulations against the observed synoptic variations. The ratio of standard devia-

520 tions range from 0.73 to 1.10, and the difference between 0.5° and 2.0° simula-
521 tions are small, while the correlation coefficients for 0.5° simulation show bet-
522 ter performance than those for 2.0° simulation. The high-resolution model cor-
523 relates well with the observations.

524 ### 3.4 Comparison with observations: Stratospheric profiles

525 There are few periodical high-precision observations of CO_2 and CH_4 in the
526 stratosphere, but observations are made over Japan about once a year using a
527 balloon-borne cryogenic sampler operated by Tohoku University, Japan
528 (Nakazawa et al., 2002; Aoki et al., 2003). In this study we compare the simu-
529 lated stratospheric profiles of CO_2 and CH_4 with the observed mean profiles
530 from the balloon-borne data over Japan. The observed mean profiles and their
531 standard deviations are obtained as follows: first the observed tracer concen-
532 trations over Sanriku (39.17°N, 141.8°E), Japan from 1985 to 2007 are aver-
533 aged in each of five height bins: below 15 km, 15–20 km, 20–25 km, 25–30 km,
534 above 30 km; then the concentrations at the highest level are shifted to match
535 observations carried out on 22 August 2012 over Taiki-cho (42.48°N, 143.42°E),
536 Japan (Nakazawa et al., 2002; Aoki et al., 2003; T. Nakazawa and S. Aoki, un-
537 published data, 2010). The simulated profiles on the same day over Sanriku
538 are compared with the averaged observed profiles (Fig. 8). The simulated pro-
539 file of CO_2 (corrected by age of air in the stratosphere, Sec. 2) is a close match
540 to the observations with no bias on the day, and the difference between simu-
541 lated and observed CO_2 profiles is within the standard deviation of the ob-
542 served CO_2. The simulated CH_4 profile also shows very good agreement with
543 the observed profiles within the observed standard deviation, though the simu-
544 lated profile tends to be smaller than the observed one at a height of about
545 100–20 hPa. Recently, De Mazière et al. (2008) compared CH_4 profiles from the
546 Atmospheric Chemistry Experiment–Fourier Transform Spectrometer (ACE–
547 FTS) launched on August 2003 with those from HALOE. They found both in-
548 struments showed similar average profiles and variability from 15 km to 70
549 km, and though ACE–FTS showed slightly higher biases compared with HA-
550 LOE, they concluded that their differences were of the order of 5% below 35
551 km (the target region of the present study) and were not significant because
552 the error bars overlapped.

Though the model–observation comparison is for only one profile due to the lack of stratospheric observations, the agreement between the simulated and observed profiles shows that nudging the model stratosphere to the climatology field of CO_2 (corrected by age of air) and CH_4 (HALOE) works quite well with no bias on the observed day or within the observed standard deviations.

3.5 Global distributions

Overall, the model successfully reproduces the observed variations of CO_2 and CH_4 as described in the previous sections. In this section, we present the latitude–longitude distributions for both the model surface level and the column-averaged dry air mole fractions. Column-averaged dry air mole fractions, XCO_2, was obtained by weighting the concentration in each layer by the air mass in that layer from the model output at 21 pressure levels; thus,

$$XCO_2 = \sum_{n=L}^{21} CO_2{}^n \times \frac{\Delta P_n}{P_{srf}}, \qquad (2)$$

where $CO_2{}^n$ is the CO_2 concentration in layer n defined at a layer center in the pressure level coordinate, L is the lowest level of the grid (surface level), P_{srf} is surface pressure, and ΔP_n is the thickness of layer n in pressure. XCH_4 is calculated in the same way.

The temporal and spatial patterns of CO_2 and CH_4 are primarily governed by seasonal cycles of the sources, sinks, and atmospheric transport. Column abundances are also sensitive to changes in surface pressure and the tropopause height (e.g., Washenfelder et al., 2003). Figures 9 and 10 show the simulated surface CO_2 and CH_4 concentrations, column CO_2 and CH_4, and their differences for January and July 2010 all at 13:00 LT, almost the same time as the GOSAT orbit descending node around 12:48 LT (Yoshida et al., 2011). Surface CO_2 concentrations in January are highest over high-emission areas such as Europe, northeast America, Siberia and Asia in the northern mid and high latitudes, and also over the equatorial regions (Africa, East South Asia, South America). Strong sinks in July are found in mid and high latitudes in Siberia and North America due to photosynthesis by land biomass in summer. Compared with the continental regions, the marine boundary layers exhibit low concentrations because of the absence of strong sources. In the

584 Southern Hemisphere, the CO_2 concentrations are relatively homogenous, ex-
585 cept for some limited continental areas such as South America. XCO_2 has less
586 variation than surface CO_2, as expected. Strong sources over China, India, and
587 Equatorial Africa and a strong sink in Siberia are still recognizable in XCO_2,
588 particularly in July. Their difference (XCO_2 – surface CO_2) is generally smaller
589 in equatorial regions due to the high tropopause height, and larger in northern
590 high latitudes due to strong sources/sinks, low tropopause height, and PBL
591 height. In July their difference is positive over mid and high northern latitudes
592 due to large sinks at the surface. Nakazawa et al. (1993) found that the ob-
593 served seasonal variation of CO_2 concentration showed a phase delay of about
594 1 month between the lower and upper troposphere by using long-term airborne
595 observations over Japan. This fact supports the positive difference between
596 XCO_2 and surface CO_2 over strong sink regions in mid and high northern lati-
597 tudes.
598 High-CH_4 regions are simulated at the surface over land both in January
599 and July, and CH_4 is higher in the Northern Hemisphere than in the Southern
600 Hemisphere throughout the year due to large CH_4 emission in the Northern
601 Hemisphere. XCH_4 exhibits the same trend as surface CH_4: relatively high in
602 the Northern Hemisphere and low in the Southern Hemisphere. High-XCH_4
603 regions, which appear over south and eastern Asia and equatorial Africa, are
604 associated with deep convection over these areas. Xiong et al. (2009) found a
605 high-CH_4 plume over south Asia in the middle to upper troposphere associated
606 with the monsoon season during July–September. These convective flows
607 transport surface CH_4 to the upper tropopause and the model can capture such
608 characteristics. While CO_2 is stable in the atmosphere, CH_4 reacts with $O(^1D)$
609 and Cl in the stratosphere in addition to chemical loss with OH radicals, creat-
610 ing a significant vertical decrease in the stratospheric concentration (Fig. 6).
611 These atmospheric sinks for CH_4 create a negative difference in (XCH_4 – sur-
612 face CH_4) except for the equatorial region where the tropopause tends to be
613 high due to strong convection.
614 Figure 11 shows the simulated surface CH_4 concentrations around Japan.
615 The high-resolution model (0.5° × 0.5°; Fig. 11a) simulates a much clearer
616 land–ocean contrast in CH_4 concentrations and synoptic-scale motions than
617 the model with a resolution of 2° × 2° (Fig. 11b). An intrusion of air mass with

low CH_4 concentrations from the Pacific is more sharply resolved in the 0.5° simulation than at 2° resolution. The 0.5° model appears to be able to resolve point sources of CH_4, such as highly populated urban areas (e.g., Tokyo), as shown by Maksyutov et al. (2008) for CO_2.

Figure 12 shows monthly zonal-mean latitudinal distributions of surface CO_2 and XCO_2, and their standard deviations at 13:00 LT, and Figure 13 those of CH_4. Zonal-mean surface CO_2 shows a strong sink centered on about 60°N in July, which then spreads toward high and low latitudes in August. The seasonal amplitude for XCO_2 is about 9 ppm, which is about half of that for surface CO_2, 15 ppm. This tendency is consistent with previous modeling studies (e.g., Olsen and Randerson, 2004). Variances are large in northern mid and southern low latitudes, reflecting activity of land biosphere. The longitudinal variations in XCO_2 are about 2 ppm at maximum.

The north-to-south gradient of the concentrations modeled at the surface level and that of XCH_4 concentrations simulated at 13:00 LT were similar in trend; i.e., the concentrations in the Northern Hemisphere are higher than those in the Southern Hemisphere. XCH_4 values at every latitude are shifted to lower concentrations due to chemical OH loss in the tropopause and the stratosphere. Small peaks in XCH_4 are found in equatorial regions throughout the year, possibly due to strong vertical transport of surface CH_4 by deep cumulus convection (e.g., Patra et al., 2009; Terao et al., 2011). CH_4 variance at the surface is high over most of the latitude band, reflecting the various CH_4 sources over land. This tendency is the same for XCH_4 but the variance is less than half the surface value. Relatively large variances in southern high latitudes might be due to the high elevation of the Antarctic Continent at over 3000 m, which makes this region susceptible to seasonal variations in tropopause height, as the stratospheric partial column of low CH_4 has a large weight.

4 Conclusions

We have developed the NIES transport model at a resolution of 0.5° × 0.5° × 47 sigma levels, driven by high-resolution meteorological data, GPV, with 0.5° × 0.5° resolution and 21 pressure levels (1000–10 hPa). This GPV-forced NIES TM has been designed to provide global high-resolution and near real-time a

652 priori CO_2 and CH_4 concentrations for the GOSAT data retrieval algorithm to
653 derive XCO_2 and XCH_4 at NIES. Since real-time fluxes of CO_2 and CH_4 are not
654 available, the flux climatologies were used with the trend adjustment to the
655 observed background concentrations. To overcome the problem of stratospheric
656 transport in the model, the stratospheric part of the model was nudged to cli-
657 matological values using three-dimensional CO_2 climatology that was adjusted
658 to observed age of air for CO_2 and long-term satellite observations from HA-
659 LOE for CH_4. We also updated the stratospheric part of the earlier version of a
660 priori error variance–covariance matrices for CO_2 and CH_4 to give more realis-
661 tic stratospheric values.
662 The model performance was assessed by comparing the model outputs
663 with available observational records of atmospheric CO_2 and CH_4 concentra-
664 tions. A large-scale, latitudinal distribution of the simulated annual mean CO_2
665 and CH_4 concentrations is found to be in good agreement with the analysis of
666 GV sites, with overall annual biases and standard deviations of –0.25 ± 1.47
667 ppm and –0.31 ± 12.57 ppb, and with RMSDs of 1.45 ppm and 12.52 ppb at 155
668 CO_2 sites and 123 CH_4 sites, respectively. In particular, pole-to-pole gradients
669 of CO_2 and CH_4 are reproduced exactly by the model with almost no biases.
670 Comparison between monthly GV CO_2 and CH_4 and the model output showed
671 that, despite large model–observation mismatch in monthly seasonal varia-
672 tions at some tower sites and some inland sites where large seasonal varia-
673 tions were observed, the model seasonal variations generally agreed well, par-
674 ticularly at oceanic and free tropospheric sites, with GV values with averaged
675 correlation coefficients of 0.87 for CO_2 and 0.53 for CH_4 in terms of seasonal
676 variations. The observed daily or discrete time series at MLO, SPO, HAT, and
677 COI are generally well reproduced by the model with statistically good perfor-
678 mance, though some discrepancies were found, possibly due to the use of cli-
679 matological fluxes. The synoptic variations at HAT and COI were reproduced
680 better by the higher-resolution model (0.5°) than the coarser-resolution model
681 (2.0°), that is, the correlation coefficients between the observation and the
682 higher-resolution model were significantly higher than those for the lower-
683 resolution model. In the stratosphere, the simulated vertical profiles and
684 growth rates agree well with the average profiles from balloon-borne observa-
685 tions over Japan within the observed standard deviations.

686 The global CO_2 and CH_4 distributions, and XCO_2 and XCH_4 obtained are
687 in qualitative agreement with previous studies. The 0.5° model can resolve
688 synoptic-scale motions and point sources better than the 2.0˚ model does. Sea-
689 sonal amplitudes in zonal-mean XCO_2 are found to be almost half those for
690 surface CO_2. Zonal-mean XCH_4 shows different features from XCO_2 because of
691 the chemical sinks in the atmosphere and its sensitivity to tropopause height.
692 These validations suggest that the model is able to reproduce fairly rea-
693 sonable global concentrations as well as synoptic variations and give confi-
694 dence in quantitative analysis of CO_2 and CH_4 cycles using the model, and its
695 use in providing a priori concentrations for satellite retrievals. This model has
696 been implemented on the GOSAT DHF system and has been run every ob-
697 served day, and the simulated results have been used for a priori concentra-
698 tions for GOSAT XCO_2 and XCH_4 retrievals. As future satellite instruments
699 like OCO-2 are expected to have smaller footprints or higher precision to ob-
700 serve greenhouse gases more precisely, the ability to simulate a priori concen-
701 trations with a higher-resolution model would be useful in reducing error in a
702 priori concentrations. Thus the updated high-resolution concentrations and
703 VCMs provided by the developed model have the potential to be powerful tools
704 for a priori of satellite data retrievals as well as for the high-resolution global
705 modeling of greenhouse gases.

706

707 **Acknowledgements**

708 This study was supported by the GOSAT project at NIES. GOSAT is a joint
709 project of the Japan Aerospace Exploration Agency (JAXA), the National Insti-
710 tute for Environmental Studies (NIES), and the Japanese Ministry of the En-
711 vironment (MoE). The extended GPV dataset for the GOSAT project was pro-
712 vided by the Japan Meteorological Agency (JMA). We appreciate the NOAA
713 ESRL GMD team for providing continuous data at MLO and SPO (PIs: Kirk
714 Thoning for CO_2 data, Ed Dlugokencky for CH_4 data), T. Nakazawa and S.
715 Aoki at Tohoku University for providing balloon-borne data, Y. Tohjima at
716 CGER/NIES for providing CH_4 data at Hateruma, and P. K. Patra at the Jap-
717 an Agency for Marine–Earth Science and Technology for providing CH_4 flux

718 data. We also thank T. Miyasaka at Fujitsu FIP Corporation for maintaining
719 NIES TM in the GOSAT DHF. We are grateful to R. Law and an anonymous
720 reviewer for useful comments to improve the manuscript. The numerical inte-
721 grations were performed on the NIES Supercomputer System (NEC SX-
722 8R/128M16).
723
724 **5 Appendix A**
725 A.1 Mass fixer
726 The mass correction is distributed proportionally to local advection tendencies
727 to conserve total tracer mass M_q

728 $$M_q = \int_0^1 \int_{-1}^1 \int_0^{2\pi} p_s \cdot (1 - 0.61 \cdot q_w) \cdot q \cdot d\lambda \cdot d(\sin\phi) \cdot d\sigma \qquad \text{(A1)}$$

729 where p_s is surface pressure, q_w is mixing ratio of water vapor, λ and ϕ indicate
730 the position in the polar coordinate system. The mass fixer constrains tracer
731 tendencies

732 $$\frac{\partial}{\partial t} M_q = 0 \qquad \text{(A2)}$$

733 on each time step. Hence the corrected tendency $\tilde{\dot{q}}$ for each tracer is

734 $$\tilde{\dot{q}} = \dot{q} \cdot \left[a_p \cdot \theta(\dot{q}) - a_n \cdot \theta(-\dot{q}) \right] \qquad \text{(A3)}$$

735 where a_p and a_n are multipliers for positive and negative tendencies, and $\theta(\dot{q})$
736 is the step function which $\theta(x)$=1 for $x \geq 0$, and $\theta(x)$=0 for $x < 0$. The condition
737 max (a_p, a_n) is enforced to keep the solution monotonic.
738
739 A.2. Cumulus convection
740 The cumulus convection is based on cumulus mass fluxes calculated in a Kuo-
741 type scheme (Grell, 1995) and modified to include entrainment and detrain-
742 ment processes on convective updrafts and downdrafts proposed by Tiedtke
743 (1989).
744 First the cloud base level σ_c is calculated by adding small perturbation to
745 humidity and temperature to levels below the σ level corresponding to 700 hPa
746 and adiabatically lifting the air parcel until the condensation occurs. The cloud
747 base σ_c is set to the lowest level where condensation would occur.
748 Then, we estimate the supply rate of moisture available for penetrative con-

vection. The horizontal moisture divergence is evaluated from winds and water vapor content. Low-level moisture convergence is calculated by integrating the horizontal moisture convergence below cloud base level and the surface evaporation. The moisture divergence term is corrected for non-zero divergence of the air mass in order to take account for deviation from the mass conservation in the wind data.

The mass flux in updraft is set to low-level moisture convergence divided by water vapor mixing ratio at cloud base. The vertical profiles of entrainment and detrainment rates are set proportional to the updraft mass flux followed by Tiedtke (1989). In the updraft air, virtual potential temperatures are estimated from the cloud base level to cloud top level. The cloud top is determined by comparing the virtual potential temperatures in the updraft and environment, for which an overshot of 3 degrees K is allowed.

The cloud with thickness of thinner than $\Delta\sigma = 0.1$ are excluded. The downdraft mass flux is set to 0.2 of that in the updraft, which is same as in Tiedtke (1989).

The tracers are transported vertically by applying a simplified explicit scheme. We assumed that the updrafts and downdrafts make only a negligibly small part of a grid column; the rest is designated as environment air. First the vertical profiles of the concentrations in the updraft and downdraft air are calculated by taking into account rates of mixing with environment air by entrainment and detrainment, and then the concentration tendencies in environment air are obtained from entrainment and detrainment rates.

A.3. Turbulent diffusion

Turbulent diffusion is temperature dependent (stability function) and is defined as follows: below PBL top, the turbulent diffusivity is set to constant value of 40 $m^2\ s^{-1}$, and above PBL, the turbulent diffusivity (K_T) is calculated by using local stability function following Hack et al. (1993):

$$K_T = \ell^2 S F_s(Ri), \qquad \text{(A4)}$$

where $\ell = 30m$ is mixing length, $S = \left| \frac{\rho g}{P_s} \frac{\partial \mathbf{V}}{\partial \sigma} \right|$ is the vertical wind shear, Ri is local Richardson number:

$$Ri = -\frac{\rho g^2}{P_s}\left(\frac{1}{S^2}\cdot\frac{\partial \ln\theta_V}{\partial\sigma}\right), \qquad \text{(A5)}$$

which is a function of the virtual potential temperature (θ_V) and the acceleration of gravity (g) . Then stability dependent function $F_s(Ri)$ is defined as:

$$F_s(Ri) = (1-18Ri)^{1/2} \quad (Ri < 0),$$

$$F_s(Ri) = 1 - \frac{Ri}{Ri_C} \quad (0 < Ri < Ri_c = 0.2), \qquad \text{(A6)}$$

$$F_s(Ri) = 0 \quad (Ri > Ri_c = 0.2).$$

A.4. Model vertical sigma levels

The 47 vertical sigma levels of the model are defined as slab centers of slab interface below:

1.000, 0.996, 0.988, 0.978, 0.968, 0.955, 0.940, 0.920, 0.900, 0.875, 0.850, 0.825, 0.800, 0.775, 0.750, 0.725, 0.700, 0.675, 0.650, 0.625, 0.600, 0.575, 0.550, 0.525, 0.500, 0.475, 0.450, 0.425, 0.400, 0.375, 0.350, 0.325, 0.300, 0.275, 0.250, 0.225, 0.200, 0.175, 0.150, 0.125, 0.100, 0.085, 0.070, 0.060, 0.050, 0.040, 0.030, 0.020.

References

Allen, M., D. Erickson, W. Kendall, J. Fu, L. Ott, and S. Pawson: The influence of internal model variability in GEOS-5 on interhemispheric CO_2 exchange, J. Geophys. Res., 117, D10107, doi:10.1029/2011JD017059, 2012.

Aoki, S., Nakazawa, T., Machida, T., Sugawara, S., Morimoto, S., Hashida, G., Yamanouchi, T., Kawamura, K., and Honda, H.: Carbon dioxide variations in the stratosphere over Japan, Scandinavia and Antarctic, Tellus B, 55, 178–186, 2003.

Belikov, D., Maksyutov, S., Miyasaka, T., Saeki, T., Zhuravlev, R., and Kiryushov, B.: Mass-conserving tracer transport modelling on a reduced latitude-longitude grid with NIES-TM, Geosci. Model Dev., 4, 207–222, doi:10.5194/gmd-4-207-2011, 2011.

Boesch, H., Baker, D., Connor, B. J., Crisp, D., and Miller, C.: Global Characterization of CO_2 Column Retrievals from Shortwave-Infrared Satellite Observations of the Orbiting Carbon Observatory-2 Mission, Remote Sens., 3, 270–34, doi:10.3390/rs3020270, 2011.

Brenkert, A. L.: Carbon dioxide emission estimates from fossil-fuel burning, hydraulic cement production, and gas flaring for 1995 on a one degree grid cell basis, Rep. NCP-058A, Carbon Dioxide Inf. Anal. Cent., Oak Ridge Natl. Lab., Oak Ridge, Tenn., http://cdiac.ornl. gov/epubs/ndp/ndp058a/ndp058a.html, 1998.

Buchwitz, M., de Beek, R., Burrows, J. P., Bovensmann, H., Warneke, T., Notholt, J., Meirink, J. F., Goede, A. P. H., Bergamaschi, P., Körner, S., Heimann, M., and Schulz, A.: Atmospheric methane and carbon dioxide from SCIAMACHY satellite data: initial comparison with chemistry and transport models, Atmos. Chem. Phys., 5, 941–962, doi:10.5194/acp-5-941-2005, 2005.

Butz, A., Guerlet, S., Hasekamp, O., Schepers, D., Galli, A., Aben, I., Frankenberg, C., Hartmann, J.-M., Tran, H., Kuze, A., Keppel-Aleks, G., Toon, G., Wunch, D., Wennberg, P., Deutscher, N., Griffith, D., Macatangay, R., Messerschmidt, J., Notholt, J., and Warneke, T.: Toward accurate CO_2 and CH_4 observations from GOSAT, Geophys. Res. Lett., 38, L14812, doi:10.1029/2011GL047888, 2011.

De Mazière, M., Vigouroux, C., Bernath, P. F., Baron, P., Blumenstock, T.,

829 Boone, C., Brogniez, C., Catoire, V., Coffey, M., Duchatelet, P., Griffith, D.,
830 Hannigan, J., Kasai, Y., Kramer, I., Jones, N., Mahieu, E., Manney, G. L., Pic-
831 colo, C., Randall, C., Robert, C., Senten, C., Strong, K., Taylor, J., Tétard, C.,
832 Walker, K. A., and Wood, S.: Validation of ACE–FTS v2.2 methane profiles
833 from the upper troposphere to the lower mesosphere, Atmos. Chem. Phys., 8,
834 2421–2435, doi:10.5194/acp-8-2421-2008, 2008.
835 Dlugokencky, E. J.: Atmospheric CH_4 daily mean data, Mauna Loa, World
836 Data Center for Greenhouse Gases, Japan Meteorol. Agency, Tokyo, Available
837 at http://ds.data.jma.go.jp/gmd/wdcgg/wdcgg.html, 2012a.
838 Dlugokencky, E. J.: Atmospheric CH_4 daily mean data, South Pole, World Data
839 Center for Greenhouse Gases, Japan Meteorol. Agency, Tokyo, Available at
840 http://ds.data.jma.go.jp/gmd/wdcgg/wdcgg.html, 2012b.
841 Dlugokencky, E. J., Harris J. M., Chung, Y. S., Tans, P. P., and Fung, I.: The
842 relationship between the methane seasonal cycle and regional sources and
843 sinks at Tae-ahn Peninsula, Korea, Atmos. Environ., 27 (14), 2115–2120, 1993.
844 Eguchi, N., Saito, R., Saeki, T., Nakatsuka, Y., Belikov, D., and Maksyutov, S.:
845 A priori covariance estimation for CO_2 and CH_4 retrievals, J. Geophys. Res.,
846 115, D10215, doi:10.1029/2009JD013269, 2010.
847 Engel, A., Möbius, T., Bönisch, H., Schmidt, U., Heinz, R., Levin, I., Atlas, E.,
848 Aoki, S., Nakazawa, T., Sugawara, S., Moore, F., Hurst, D., Elkins, J., Schauf-
849 fler, S., Andrews, A., and Boering, K.: Age of stratospheric air unchanged with-
850 in uncertainties over the past 30 years, Nat. Geosci., 2, 28–31,
851 doi:10.1038/ngeo388, 2009.
852 Fung, I., John, J., Lerner, J., Matthews, E., Prather, M., Steele, L. P., and Fra-
853 ser, P. J.: Three-dimensional model synthesis of the global methane cycle, J.
854 Geophys. Res., 96, 13033–13065, 1991.
855 Geels, C., Doney, S., Dargaville, R., Brandt, J., and Christensen, J. H.: Investi-
856 gating the sources of synoptic variability in atmospheric CO_2 measurements
857 over the Northern Hemisphere continents: A regional model study, Tellus B,
858 56, 35–50, 2004.
859 Geels, C., Gloor, M., Ciais, P., Bousquet, P., Peylin, P., Vermeulen, A. T., Dar-
860 gaville, R., Aalto, T., Brandt, J., Christensen, J. H., Frohn, L. M., Haszpra, L.,
861 Karstens, U., Rödenbeck, C., Ramonet, M., Carboni, G., and Santaguida, R.:
862 Comparing atmospheric transport models for future regional inversions over

Europe – Part 1: mapping the atmospheric CO_2 signals, Atmos. Chem. Phys., 7, 3461–3479, doi:10.5194/acp-7-3461-2007, 2007.

GLOBALVIEW-CH_4: Cooperative Atmospheric Data Integration Project - Methane. CD-ROM, NOAA/CMDL, Boulder, Colorado [Also available on Internet via anonymous FTP to ftp.cmdl.noaa.gov, Path: ccg/ch4/GLOBALVIEW], 2009.

GLOBALVIEW-CO_2: Cooperative Atmospheric Data Integration Project - Carbon Dioxide. CD-ROM, NOAA/CMDL, Boulder, Colorado [Also available on Internet via anonymous FTP to ftp.cmdl.noaa.gov, Path: ccg/co2/GLOBALVIEW], 2009.

Grell, G., J. Dudhia, and D. Stauffer: Description of the Fifth- Generation Penn State/NCAR Mesoscale Model (MM5), NCAR/TN- 398. NCAR, Boulder, Colo., USA, 1995.

Gurney, K. R., Law, R. M., Denning, A. S., Rayner, P. J., Baker, D., Bousquet, P., Bruhwiler, L., Chen, Y.-H., Ciais, P., Fan, S., Fung, I. Y., Gloor, M., Heimann, M., Higuchi, K., John, J., Maki, T., Maksyutov, S., Masarie, K., Peylin, P., Prather, M., Pak, B. C., Randerson, J., Sarmiento, J., Taguchi, S., Takahashi, T., and Yuen, C.-W.: Towards robust regional estimates of CO_2 sources and sinks using atmospheric transport models, Nature, 415, 626–630, 2002.

Gurney, K. R., Denning, A. S., Rayner, P., Pak. B., Baker, D., Bousquet, P., Bruhwiler, L., Chen, Y.-H., Ciais, P., Fung, I. Y., Heimann, M., Higuchi, K., John, J., Maki, T., Maksyutov, S., Peylin, P., Prather, M., Taguchi, S.: Transcom 3 inversion intercomparison: Model mean results for the estimation of seasonal carbon sources and sinks, Global Biogeochem. Cycles, 18, GB1010, doi:10.1029/2003GB002111, 2004.

Hack, J. J., Boville, B. A., Briegleb, B. P., Kiehl, J. T., Rasch, P. J. and D. L. Williamson: Description of the NCAR community climate model (CCM2), NCAR/TN-382, NCAR, Boulder, Colo., USA, 1993.

Higuchi, K., Murayama, S., and Taguchi, S.: Quasi-decadal variation of the atmospheric CO_2 seasonal cycle due to atmospheric circulation changes: 1979–1998, Geophys. Res. Lett., 29(8), 1173, doi:10.1029/2001GL013751, 2002.

Japan Aerospace Exploration Agency, National Institute for Environmental Studies, and Ministry of the Environment: GOSAT/IBUKI Data Users Handbook, 1st Edition,

https://data.gosat.nies.go.jp/GosatUserInterfaceGateway/guig/doc/GOSAT_HB_E_1stEdition_for_HP.pdf, 2011.

JMA: Outline of the operational numerical weather prediction at the Japan Meteorological Agency. (Appendix to the WMO Tech- nical Progress Report on the Global Data-Processing and Fore- casting System and Numerical Weather Prediction). Japan Mete- orological Agency, 194, available at: http://www.jma.go.jp/jma/ jma-eng/jma-center/nwp/outline-nwp/index.htm, 2007.

Kuze, A., Suto, H., Nakajima, M., and Hamazaki, T.: Thermal and near infrared sensor for carbon observation Fourier-transform spectrometer on the Greenhouse Gases Observing Satellite for greenhouse gases monitoring, Appl. Optics, 48, 6716–6733, 2009.

Law, R. M., Peters, W., Rödenbeck, C., Aulagnier, C., Baker, I., Bergmann, D. J., Bousquet, P., Brandt, J., Bruhwiler, L., Cameron-Smith, P. J., Christensen, J. H., Delage, F., Denning, A. S., Fan, S., Geels, C., Houweling, S., Imasu, R., Karstens, U., Kawa, S. R., Kleist, J., Krol, M. C., Lin, S. J., Lokupitiya, R., Maki, T., Maksyutov, S., Niwa, Y., Onishi, R., Parazoo, N., Patra, P. K., Pieterse, G., Rivier, L., Satoh, S., Serrar, S., Taguchi, S., Takigawa, M., Vautard, R., Vermeulen, A. T., and Zhu, Z.: TransCom model simulations of hourly atmospheric CO_2: Experimental overview and diurnal cycle results for 2002, Global Biogeochem. Cycles, 22, GB3009, doi:10.1029/2007GB003050, 2008.

Maksyutov, S., Patra, P. K., Onishi, R., Saeki, T., and Nakazawa, T.: NIES/FRCGC global atmospheric tracer transport model: Description, validation, and surface sources and sinks inversion. J. Earth Simulator, 9, 3–18, 2008.

Masarie, K., and Tans, P. P.: Extension and integration of atmospheric carbon dioxide data into a globally consistent measurement record, Journal of Geophysical Research, 100(D6), 11593–11610, doi:10.1029/95JD00859, 1995.

Nakazawa, T., Morimoto, S., Aoki, S., and Tanaka, M.: Time and space variations of the carbon isotopic ratio of the tropospheric carbon dioxide over Japan, Tellus B, 45, 258–274, 1993.

Nakazawa, T., Ishizawa, M., Higuchi, K., and Trivett, N.: Two curve fitting methods applied to CO_2 flask data, Environmetrics, 8, 197–218, 1997.

Nakazawa, T., Aoki, S., Kawamura, K., Saeki, T., Sugawara, S., Honda, H.,

931 Hashida, G., Morimoto, S., Yoshida, N., Toyoda, S., Makide, Y., Shirai, T.: Var-
932 iations of stratospheric trace gases measured using a balloon-borne cryogenic
933 sampler, Advances in Space Research, 30 (5), 1349–1357, 2002.
934 O'Dell, C. W., Connor, B., Bösch, H., O'Brien, D., Frankenberg, C., Castano, R.,
935 Christi, M., Eldering, D., Fisher, B., Gunson, M., McDuffie, J., Miller, C. E.,
936 Natraj, V., Oyafuso, F., Polonsky, I., Smyth, M., Taylor, T., Toon, G. C., Wenn-
937 berg, P. O., and Wunch, D.: The ACOS CO_2 retrieval algorithm – Part 1: De-
938 scription and validation against synthetic observations, Atmos. Meas. Tech., 5,
939 99–121, doi:10.5194/amt-5-99-2012, 2012.
940 Olivier, J. G. J., and Berdowski, J. J. M.: Global emissions sources and sinks,
941 in: The Climate System, A. A. Balkema Publishers/Swets and Zeitlinger Pub-
942 lishers, Lisse, The Netherlands, 33–78, 2001.
943 Olsen, S. C., and Randerson, J. T.: Differences between surface and column
944 atmospheric CO_2 and implications for carbon cycle research, J. Geophys. Res.,
945 109, D02301, doi:10.1029/2003JD003968, 2004.
946 Oshchepkov, S., Bril, A., Maksyutov, S., and Yokota, T.: Detection of optical
947 path in spectroscopic space-based observations of greenhouse gases: Applica-
948 tion to GOSAT data processing, J. Geophys. Res., 116, D14304,
949 doi:10.1029/2010JD015352, 2011.
950 Park, J. H., Russell, J. M., III, Gordley, L. L., Drayson, S. R., Benner, D. C.,
951 McInerney, J. M., Gunson, M. R., Toon, G. C., Sen, B., Blavier, J.-F., Webster,
952 C. R., Zipf, E. C., Erdman, P., Schmidt, U., Schiller, C.: Validation of Halogen
953 Occultation Experiment CH_4 measurements from the UARS, J. Geophys. Res.,
954 101(D6), 10,183–10,203, doi:10.1029/95JD02736, 1996.
955 Patra, P. K., and Maksyutov, S.: Incremental approach to the optimal network
956 design for CO_2 surface source inversion, Geophys. Res. Lett., 29(10), 1459,
957 2002.
958 Patra, P. K., Maksyutov, S., Sasano, Y., Nakajima, H., Inoue, G., and Nakaza-
959 wa, T.: An evaluation of CO_2 observations with Solar Occultation FTS for In-
960 clined-Orbit Satellite sensor for surface source inversion, J. Geophys. Res., 108
961 (D24), 4759, 2003.
962 Patra, P. K., Ishizawa, M., Maksyutov, S., Nakazawa, T., and Inoue, G.: Role of
963 biomass burning and climate anomalies for land–atmosphere carbon fluxes
964 based on inverse modeling of atmospheric CO_2, Global Biogeochem. Cycles, 19,

965 GB3005, 2005a.
966 Patra, P. K., Maksyutov, S., and Nakazawa, T.: Analysis of atmospheric CO_2
967 growth rates at Mauna Loa using inverse model derived CO_2 fluxes, Tellus B,
968 57, 357–365, 2005b.
969 Patra, P. K., Law, R. M., Peters, W., Rödenbeck, C., Takigawa, M., Aulagnier,
970 C., Baker, I., Bergmann, D. J., Bousquet, P., Brandt, J., Bruhwiler, L., Camer-
971 on-Smith, P. J., Christensen, J. H., Delage, F., Denning, A. S., Fan, S., Geels,
972 C., Houweling, S., Imasu, R., Karstens, U., Kawa, S. R., Kleist, J., Krol, M. C.,
973 Lin, S.-J., Lokupitiya, R., Maki, T., Maksyutov, S., Niwa, Y., Onishi, R., Para-
974 zoo, N., Pieterse, G., Rivier, L., Satoh, M., Serrar, S., Taguchi, S., Vautard, R.,
975 Vermeulen, A. T., and Zhu, Z.: TransCom model simulations of hourly atmos-
976 pheric CO_2: Analysis of synoptic-scale variations for the period 2002–2003,
977 Global Biogeochem. Cycles, 22, GB4013, doi:10.1029/2007GB003081, 2008.
978 Patra, P. K., Takigawa, M., Ishijima, K., Choi, B.-C., Cunnold, D.,
979 Dlugokencky, E. J., Fraser, P., Gomez-Pelaez, A. J., Goo, T.-Y., Kim, J.-S.,
980 Krummel, P., Langenfelds, R., Meinhardt, F., Mukai, H., O'Doherty, S., Prinn,
981 R. G., Simmonds, P., Steele, P., Tohjima, Y., Tsuboi, K., Uhse, K., Weiss, R.,
982 Worthy, D., and Nakazawa, T.: Growth rate, seasonal, synoptic and diurnal
983 variations in lower atmospheric methane and its budget, J. Meteorol. Soc. Jpn.,
984 87(4), 635–663, 2009.
985 Patra, P. K., Houweling, S., Krol, M., Bousquet, P., Belikov, D., Bergmann, D.,
986 Bian, H., Cameron-Smith, P., Chipperfield, M. P., Corbin, K., Fortems-Cheiney,
987 A., Fraser, A., Gloor, E., Hess, P., Ito, A., Kawa, S. R., Law, R. M., Loh, Z.,
988 Maksyutov, S., Meng, L., Palmer, P. I., Prinn, R. G., Rigby, M., Saito, R., and
989 Wilson, C.: TransCom model simulations of CH_4 and related species: linking
990 transport, surface flux and chemical loss with CH4 variability in the tropo-
991 sphere and lower stratosphere, Atmos. Chem. Phys., 11, 12813–12837,
992 doi:10.5194/acp-11-12813-2011, 2011.
993 Pérez-Landa, G., Ciais, P., Sanz, M. J., Gioli, B., Miglietta, F., Palau, J. L.,
994 Gangoiti, G., and Millán, M. M.: Mesoscale circulations over complex terrain in
995 the Valencia coastal region, Spain – Part 1: Simulation of diurnal circulation
996 regimes, Atmos. Chem. Phys., 7, 1835–1849, doi:10.5194/acp-7-1835-2007,
997 2007a.
998 Pérez-Landa, G., Ciais, P., Gangoiti, G., Palau, J. L., Carrara, A., Gioli, B.,

999 Miglietta, F., Schumacher, M., Millan, M. M., and Sanz, M. J.: Mesoscale circu-
1000 lations over complex terrain in the Valencia coastal region, Spain–Part 2:
1001 Modeling CO_2 transport using idealized surface fluxes, Atmos. Chem. Phys., 7,
1002 1851–1868, doi:10.5194/acp-7-1851-2007, 2007b.
1003 Randerson, J. T., Thompson, M. V., Conway, T. J., Fung, I. Y., and Field, C. B.:
1004 The contribution of terrestrial sources and sinks to trends in the seasonal cycle
1005 of atmospheric carbon dioxide, Global Biogeochem. Cycles, 11, 535–560, 1997.
1006 Russell, J. M., III, Gordley, L. L., Park, J. H., Drayson, S. R., Hesketh, D. H.,
1007 Cicerone, R. J., Tuck, A. F., Frederick, J. E., Harries, J. E., and Crutzen, P. J.:
1008 The Halogen Occultation Experiment, J. Geophys. Res., 98 (D6), 10777–10797,
1009 1993.
1010 Saito, R., Houweling, S., Patra, P. K., Belikov, D., Lokupitiya, R., Niwa, Y.,
1011 Chevallier, F., Saeki, T., and Maksyutov, S.: TransCom satellite intercompari-
1012 son experiment: Construction of a bias corrected atmospheric CO_2 climatology,
1013 J. Geophys. Res., 116, D21120, doi:10.1029/2011JD016033, 2011.
1014 Saitoh, N., Imasu, R., Ota, Y., and Niwa, Y.: CO_2 retrieval algorithm for the
1015 thermal infrared spectra of the Greenhouse Gases Observing Satellite: Poten-
1016 tial of retrieving CO_2 vertical profile from high-resolution FTS sensor, J. Ge-
1017 ophys. Res., 114, D17305, doi:10.1029/2008JD011500, 2009.
1018 Schepers, D., Guerlet, S., Butz, A., Landgraf, J., Frankenberg, C., Hasekamp,
1019 O., Blavier, J.-F., Deutscher, N.M., Griffith, D.W.T., Hase, F., Kyro, E., Morino,
1020 I., Sherlock, V., Sussmann, R., and Aben, I.: Methane retrievals from Green-
1021 house Gases Observing Satellite (GOSAT) shortwave infrared measurements:
1022 Performance comparison of proxy and physics retrieval algorithms, J. Geophys.
1023 Res., 117, D10307, doi:10.1029/2012JD017549, 2012.
1024 Spivakovsky, C. M., Logan, J. A., Montzka, S. A., Balkanski, Y. J., Foreman-
1025 Fowler, M., Jones, D. B. A., Horowitz, L. W., Fusco, A. C., Brenninkmeijer, C.
1026 A. M., Prather, M. J., Wofsy, S. C., and McElroy, M. B.: Three dimensional
1027 climatological distribution of tropospheric OH: Update and evaluation, J. Ge-
1028 ophys. Res., 105, 8931–8980, 2000.
1029 Takahashi, T., Sutherland, S. C., Sweeney, C., Poisson, A., Metzl, N., Tilbrook,
1030 B., Bates, N., Wanninkhof, R., Feely, R. A., Sabine, C., Olafsson, J., and Nojiri,
1031 Y.: Global sea–air CO_2 flux based on climatological surface ocean pCO_2, and
1032 seasonal biological and temperature effects, Deep Sea Res., Part II, 49, 1601–

1622, 2002.
Terao, Y., Mukai, H., Nojiri, Y., Machida, T., Tohjima, Y., Saeki, T., and Maksyutov, S.: Interannual variability and trends in atmospheric methane over the western Pacific from 1994 to 2010, J. Geophys. Res., 116, D14303, doi:10.1029/2010JD015467, 2011.
Thoning, K. W.: Atmospheric CO_2 daily mean data, Mauna Loa, World Data Center for Greenhouse Gases, Japan Meteorol. Agency, Tokyo, Available at http://ds.data.jma.go.jp/gmd/wdcgg/wdcgg.html, 2012a.
Thoning, K. W.: Atmospheric CO_2 daily mean data, South Pole, World Data Center for Greenhouse Gases, Japan Meteorol. Agency, Tokyo, Available at http://ds.data.jma.go.jp/gmd/wdcgg/wdcgg.html, 2012b.
Tiedtke, M: A comprehensive mass flux scheme for cumulus parameterization in large-scale models, Mon.Wea. Rev. 117, 1779–1800, 1989.
Tohjima, Y., Machida, T., Utiyama, M., Katsumoto, M., Fujinuma, Y., and Maksyutov, S.: Analysis and presentation of in situ atmospheric methane measurements from Cape Ochi-ishi and Hateruma Island, J. Geophys. Res., 107, 4148, doi:10.1029/2001JD001003, 2002.
Tohjima, Y., Mukai, H., Hashimoto, S., and Patra, P. K.: Increasing synoptic scale variability in atmospheric CO2 at Hateruma Island associated with increasing East-Asian emissions, Atmos. Chem. Phys., 10, 453-462, doi:10.5194/acp-10-453-2010, 2010.
Washenfelder, R. A., Wennberg, P. O., and Toon, G. C.: Tropospheric methane retrieved from ground-based near-IR solar absorption spectra, Geophys. Res. Lett., 30(23), 2226, doi:10.1029/2003GL017969, 2003.
Xiong, X., Houweling, S., Wei, J., Maddy, E., Sun, F., and Barnet, C.: Methane plume over south Asia during the monsoon season: satellite observation and model simulation, Atmos. Chem. Phys., 9, 783–794, doi:10.5194/acp-9-783-2009, 2009.
Wang, J.-W., Denning, A. S., Lu, L., Baker, I. T., Corbin, K. D., and Davis, K. J.: Observations and simulations of synoptic, regional, and local variations in atmospheric CO2, J. Geophys. Res., 112, D04108, doi:10.1029/2006JD007410, 2007.
Yokota, Y., Yoshida, Y., Eguchi, N., Ota, Y., Tanaka, T., Watanabe, H., and Maksyutov, S.: Global Concentrations of CO_2 and CH_4 Retrieved from GOSAT:

First Preliminary Results, SOLA, 2009, Vol. 5, 160–163, doi:10.2151/sola.2009-041, 2009.

Yoshida, Y., Ota, Y., Eguchi, N., Kikuchi, N., Nobuta, K., Tran, H., Morino, I., and Yokota, T.: Retrieval algorithm for CO_2 and CH_4 column abundances from short-wavelength infrared spectral observations by the Greenhouse gases observing satellite, Atmos. Meas. Tech., 4, 717–734, doi:10.5194/amt-4-717-2011, 2011.

1075 **Table 1.** Statistics to show the model performance against GLOBALVIEW
1076 analyses of CO_2 and CH_4: annual-mean biases and seasonal variations.

Tracer	Site type*1	Number of sites	Annual mean		Seasonal variation		
			Biases and standard deviations	RMSD*2	RSTD*3	Correlation coefficients*4	CRMSD*5
CO_2	Oceanic	56	–0.04 ± 1.16	1.15	0.83	0.97	0.28
	Land	45	–0.31 ± 1.74	1.74	0.82	0.92	0.41
	Tower	9	1.80 ± 2.24	2.77	0.66	0.65	0.76
	Free tropos.	45	–0.95 ± 0.38	1.02	0.80	0.94	0.36
	Total	155	–0.25 ± 1.47	1.45	0.78	0.87	0.50
CH_4	Oceanic	46	0.72 ± 8.20	8.15	1.14	0.70	0.84
	Land	45	2.05 ± 17.66	17.58	0.43	0.43	1.21
	Tower	1	16.13	16.13	1.58	0.025	1.83
	Free tropos.	31	–5.79 ± 5.86	8.17	1.07	0.63	0.89
	Total	123	–0.31 ± 12.57	12.52	1.20	0.53	1.08

1077 *1 Site types: the same as those defined in Fig. 2.

1078 *2 Root-mean-square differences (RMSD)

1079 *3 Ratio of standard deviation (SD), which is calculated by dividing the model
1080 SD by the observed SD.

1081 *4 Pearson's correlation coefficient.

1082 *5 Centered pattern root-mean-square differences (CRMSD), which is a
1083 measure of the distance between model and observation.

1084

Table 2. Statistics to show the model performance against continuous measurements for daily-mean CO_2 and CH_4 at HAT (Hateruma), Cape Ochi-ishi (COI), MLO (Mauna Loa), and SPO (South Pole). Observed CH_4 data at SPO are discrete data, and the simulated results corresponding to the measurement date are used for the comparisons. Statistics are defined as in Table 1.

Tracers	Site	Time interval of comparisons	Period of comparisons	Number of data	RSTD	Correlation coefficients	Overall bias	CRMSD
CO_2	HAT	Daily	1 Jan. 2007 – 30 Aug. 2011	1638	0.82	0.90	–0.29	0.44
	COI	Daily	1 Jan. 2007 – 31 Aug. 2011	1644	0.59	0.73	–0.44	0.70
	MLO	Daily	1 Jan. 2007 – 31 Dec. 2010	1351	0.88	0.96	–0.41	0.28
	SPO	Daily	1 Jan. 2007 – 31 Dec. 2010	1439	1.12	0.98	0.73	0.25
CH_4	HAT	Daily	1 Jan. 2007 – 31 Dec. 2010	1421	0.95	0.83	2.44	0.57
	MLO	Daily	1 Jan. 2007 – 31 Dec. 2010	1377	0.82	0.59	–9.83	0.84
	SPO	Event	1 Jan. 2007 – 31 Dec. 2010	191	0.92	0.96	–1.19	0.30

1092

Table 3. Correlation coefficients and Ratio of standard deviation between synoptic variations in observed and simulated CO_2 and CH_4 concentrations at HAT (Hateruma), Cape Ochi-ishi (COI). "0.5°" and "2.0°" indicate 0.5-degree simulation and 2.0-degree simulation, respectively. Statistics are defined as in Table 1.

Tracers	Site	Time interval of comparisons	Period of comparisons	Number of data	Correlation coefficient		RSTD	
					0.5°	2.0°	0.5°	2.0°
CO_2	HAT	Daily	1 Jan. 2008 – 31 Dec. 2010	1064	0.72	0.41	0.73	0.82
	COI	Daily	1 Jan. 2008 – 31 Dec. 2010	1644	0.62	0.55	0.85	0.71
CH_4	HAT	Daily	1 Jan. 2008 – 31 Dec. 2010	1057	0.85	0.56	1.08	1.10

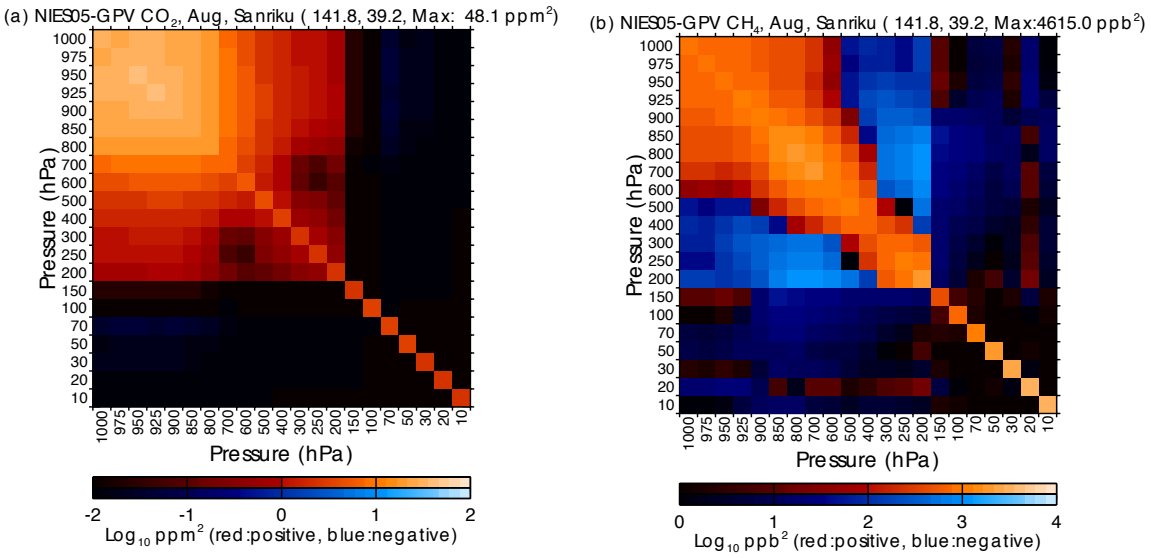

Fig. 1. A priori error variance–covariance matrices of (a) CO_2 and (b) CH_4 over Sanriku, Japan (141.8°E, 39.2°E) in August at 21 pressure levels from 1000 to 10 hPa. Color scales are logarithmic, with ranges of 0.01–100 ppm^2 for CO_2 and 1–10000 ppb^2 for CH_4. Warm and cold colors indicate positive and negative correlations, respectively. Dark and light colors indicate small and

1106 large variance–covariance values, respectively.

1107

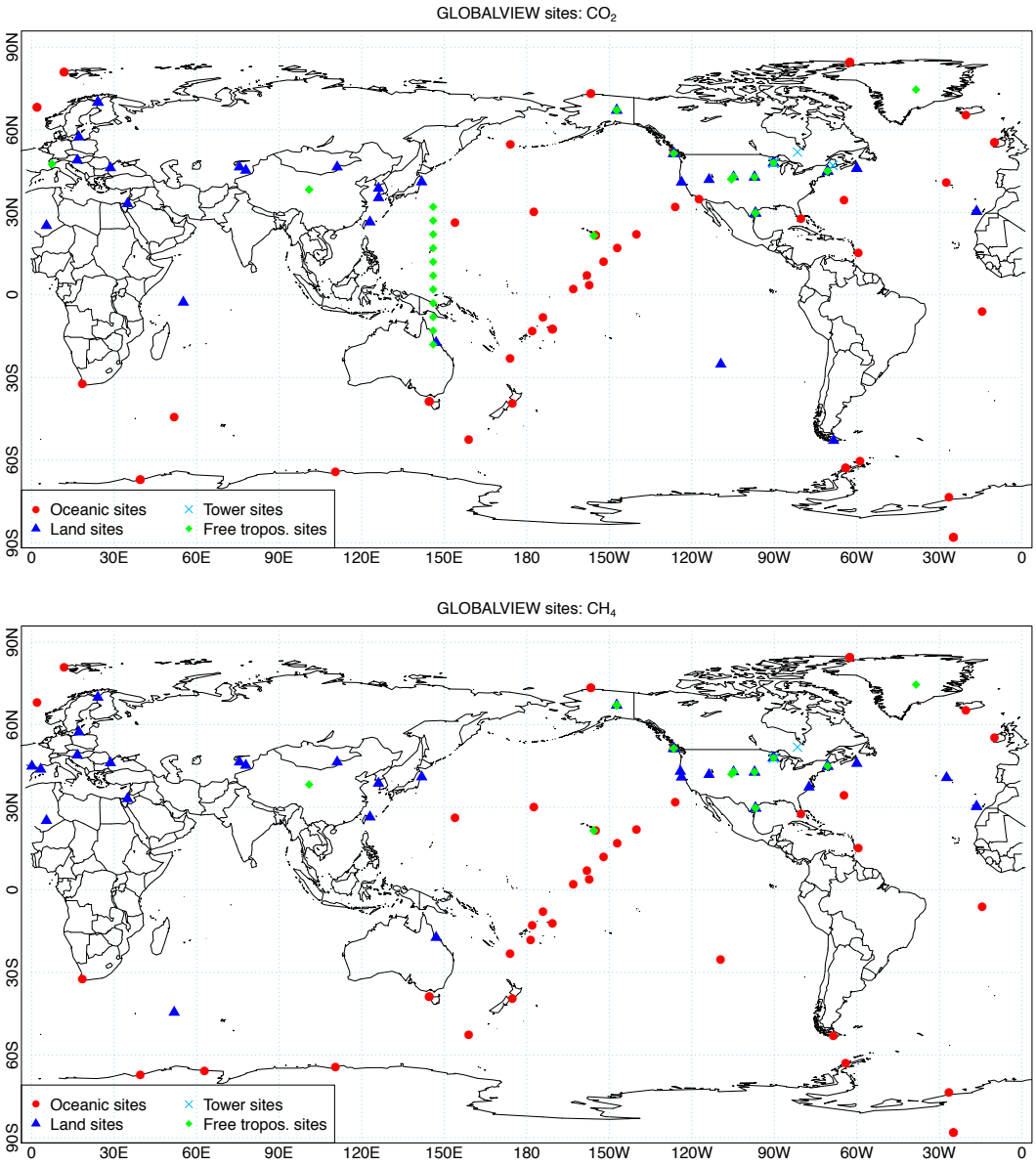

1108

1109 **Fig. 2.** GLOBALVIEW site locations used for the comparisons of CO_2 (top)
1110 and of CH_4 (bottom) for the year 2008. "Oceanic"; sites with marine-boundary-
1111 layer (MBL) marks in the GV dataset (gv_table.co2 and gv_table.ch4); "land",
1112 sites below 3000 m which are neither MBL sites nor tower sites; "tower", tower
1113 sites with sampling platform code "3" in GV file names; "free tropos.", free
1114 troposphere sites located above 3000 m and marked as non-MBL sites, mostly
1115 airborne observational points.

1116

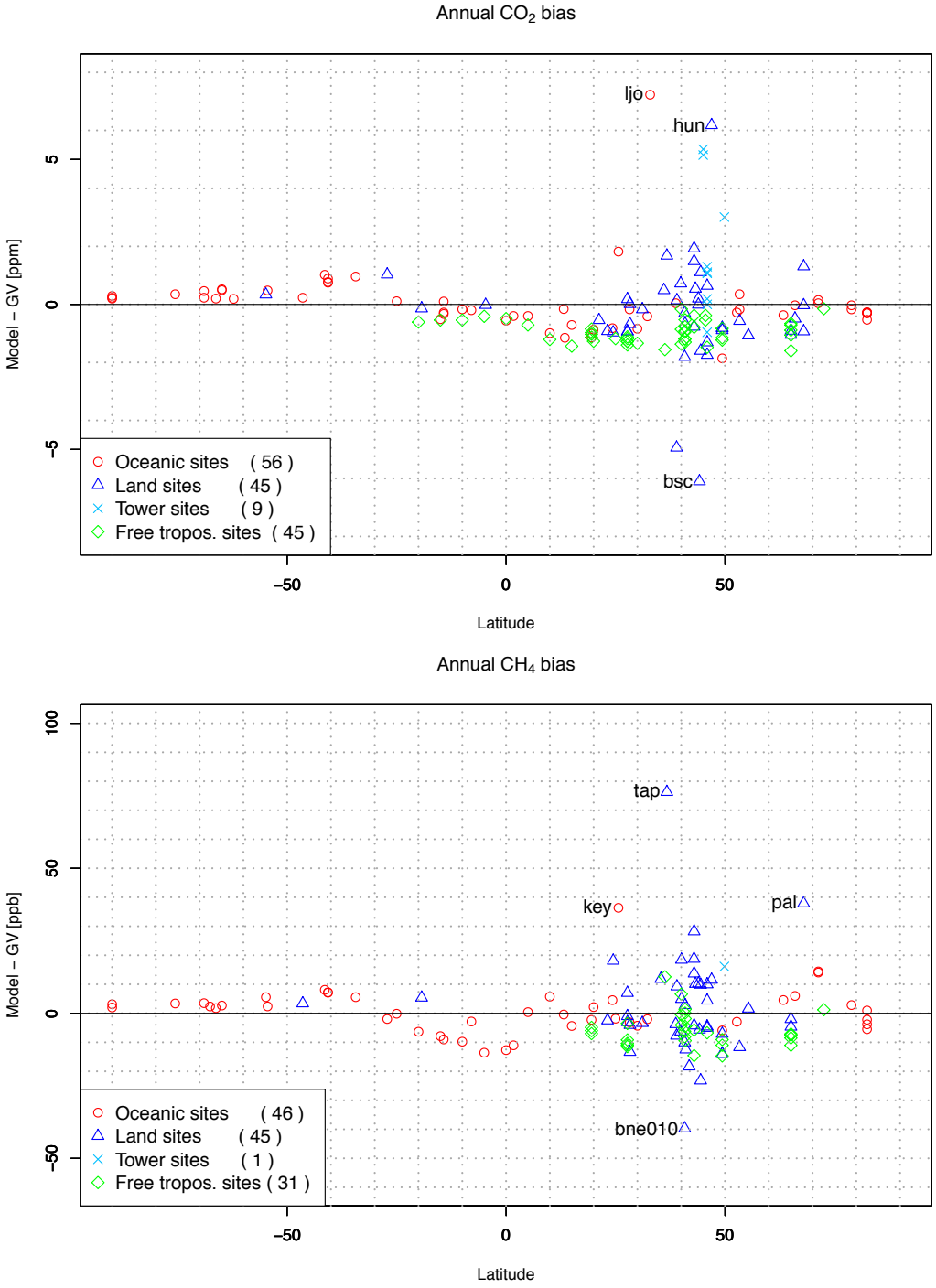

1117

1118 **Fig. 3.** Latitudinal distributions of differences in annual mean between the
1119 simulated and GV data for CO_2 (top) and CH_4 (bottom) at GV monitoring sites

for the year 2008. The simulated results at 13.00–16.00 LT were used for the comparison. Letters in the plot represent the GV site code. Site types in the legend are the same as those defined in Fig. 2. Numbers in legend parentheses indicate the numbers of GV sites used for the analysis.

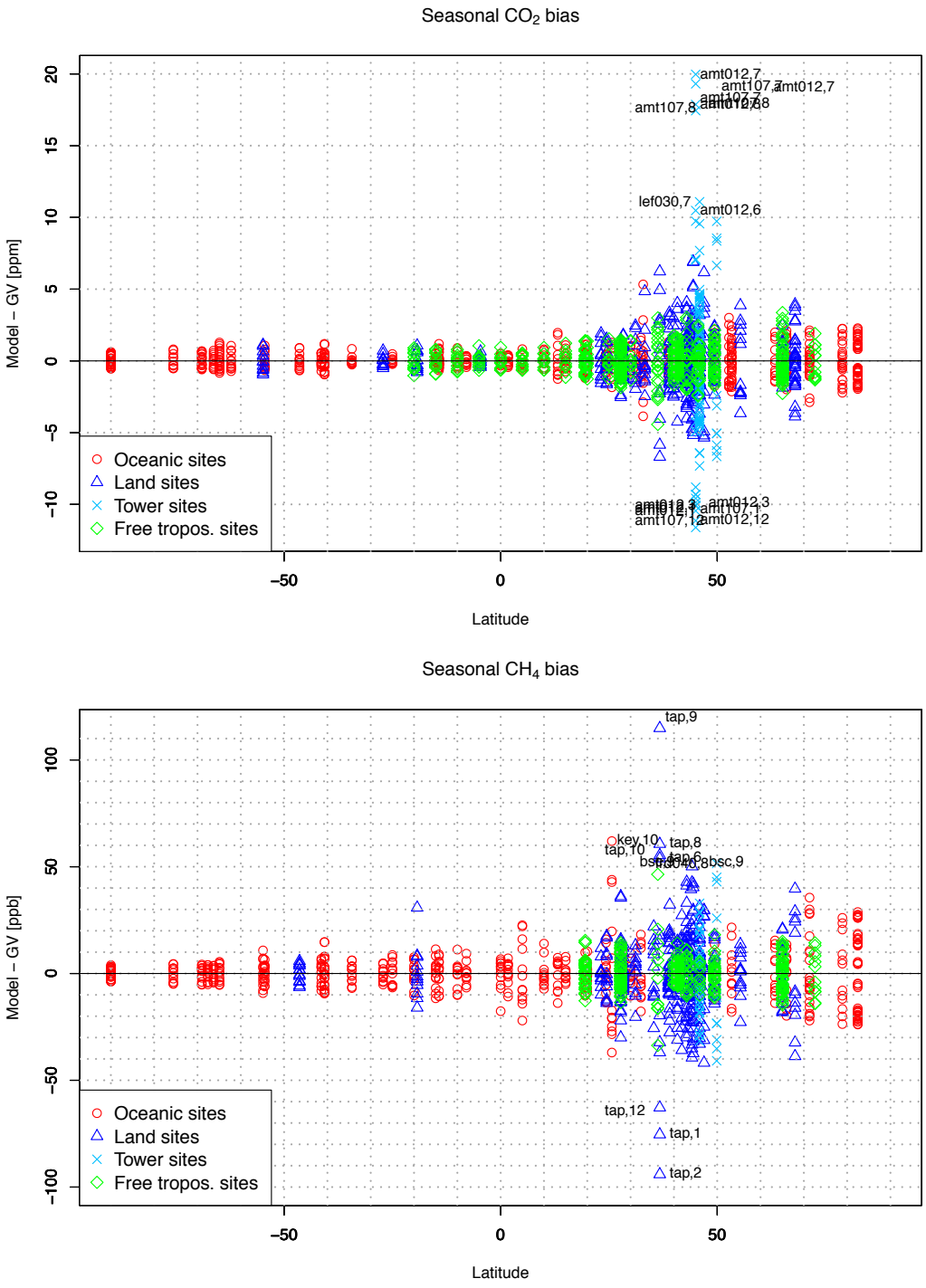

1125

1126 **Fig. 4.** Same as Fig. 3, but for monthly biases for CO_2 (top) and CH_4 (bottom).
1127 Letters and numbers in the plot represent GV site code and month, respective-

ly.

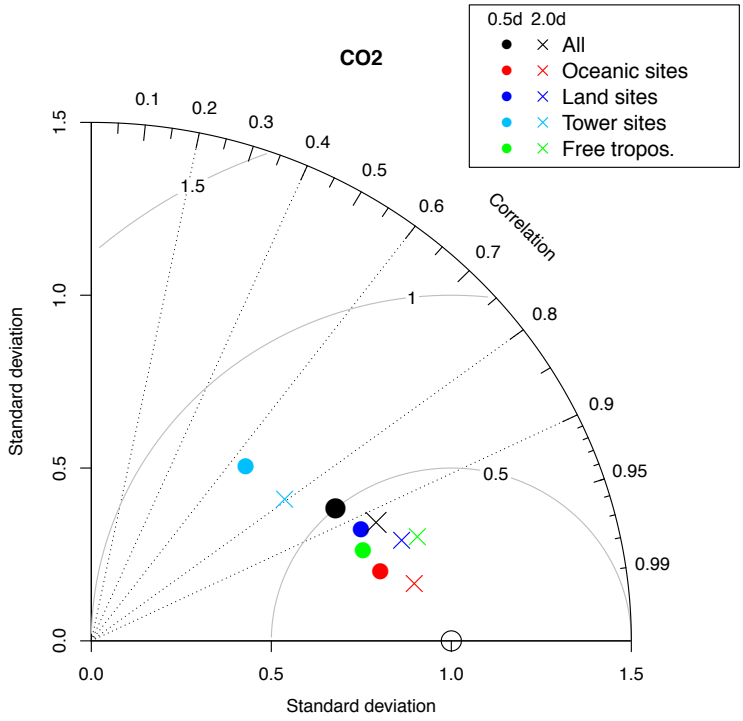

1130

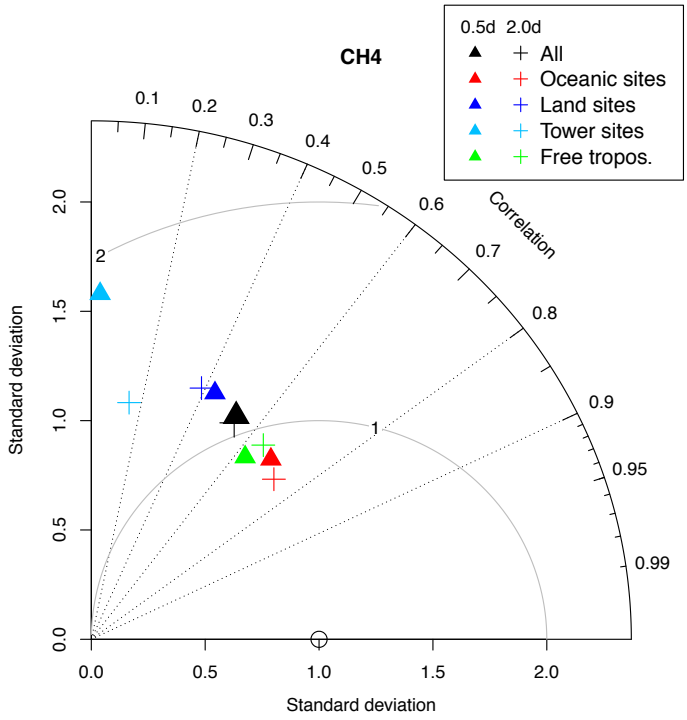

1131

1132 **Fig. 5.** Normalized Taylor diagram showing a statistical comparison (Pear-
1133 son's correlation coefficient, normalized standard deviation, and centered root-
1134 mean-square difference) between simulated CO_2 (top) and CH_4 (bottom), and
1135 GV analysis, for monthly seasonal variations. "0.5d" and "2.0d" in legends in-
1136 dicate 0.5-degree simulation and 2.0-degree simulation, respectively.

1137

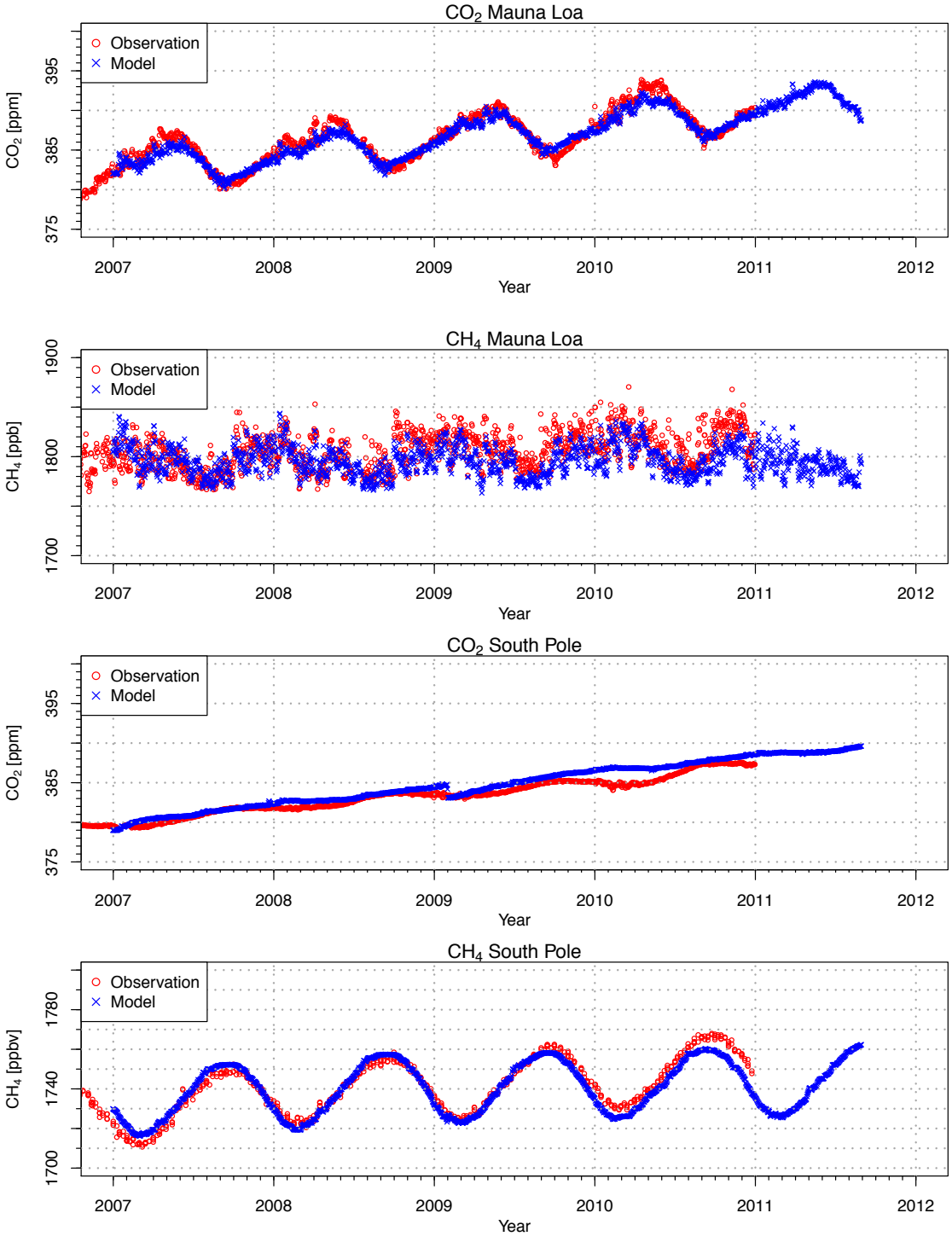

1138

1139 **Fig. 6.** Observed and simulated time series of daily mean CO_2 and CH_4 con-
1140 centrations at Mauna Loa, South Pole, and Hateruma sites, and CO_2 concen-
1141 tration at Ochi-ishi sites. CH_4 observations at South Pole are discrete data and
1142 are plotted directly; quasi-continuous data at the other sites and 3-hourly

model output are daily averages. "0.5d" and "2.0d" in legends for Hateruma and Ochi-ishi sites indicate 0.5-degree simulation and 2.0-degree simulation, respectively. A gap in the simulated CO_2 at SPO at the end of January 2009 is due to the offset correction (see text).

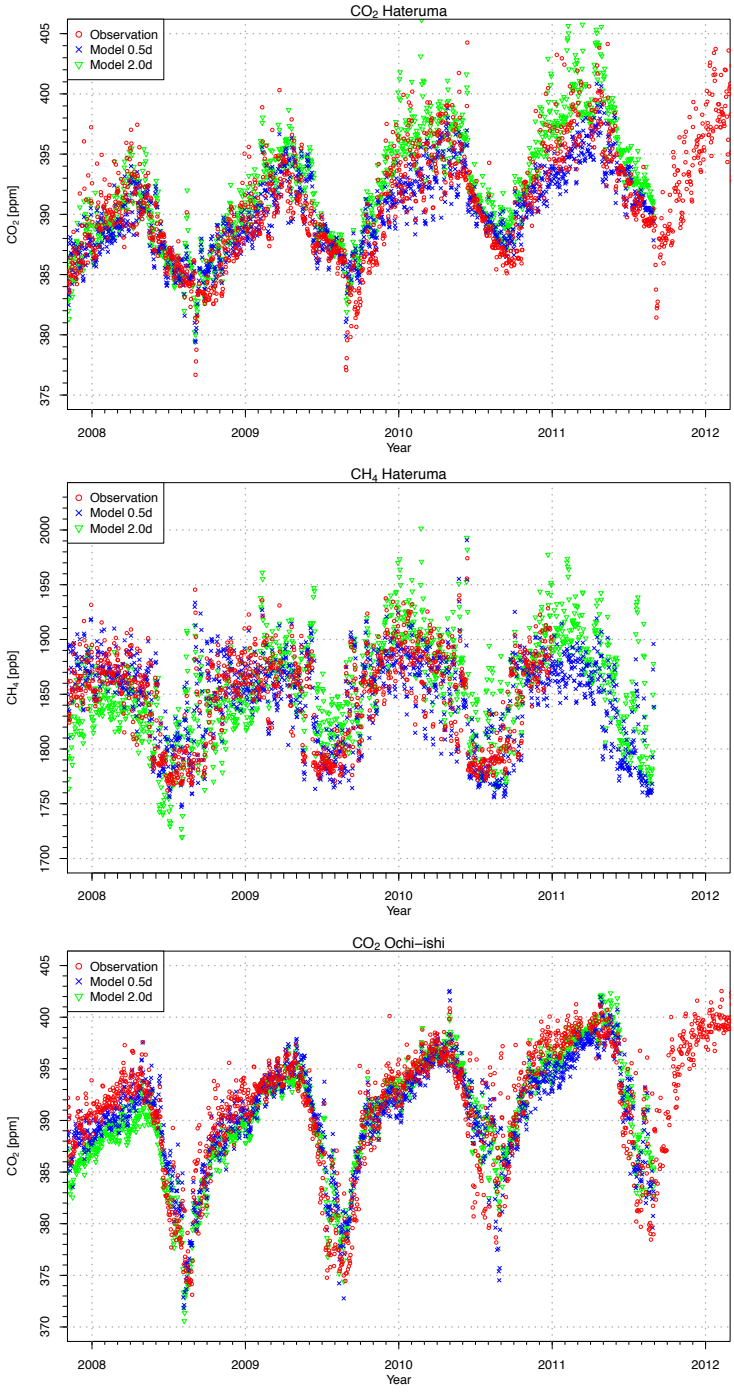

1147

1148 **Fig. 6.** Continued

1149

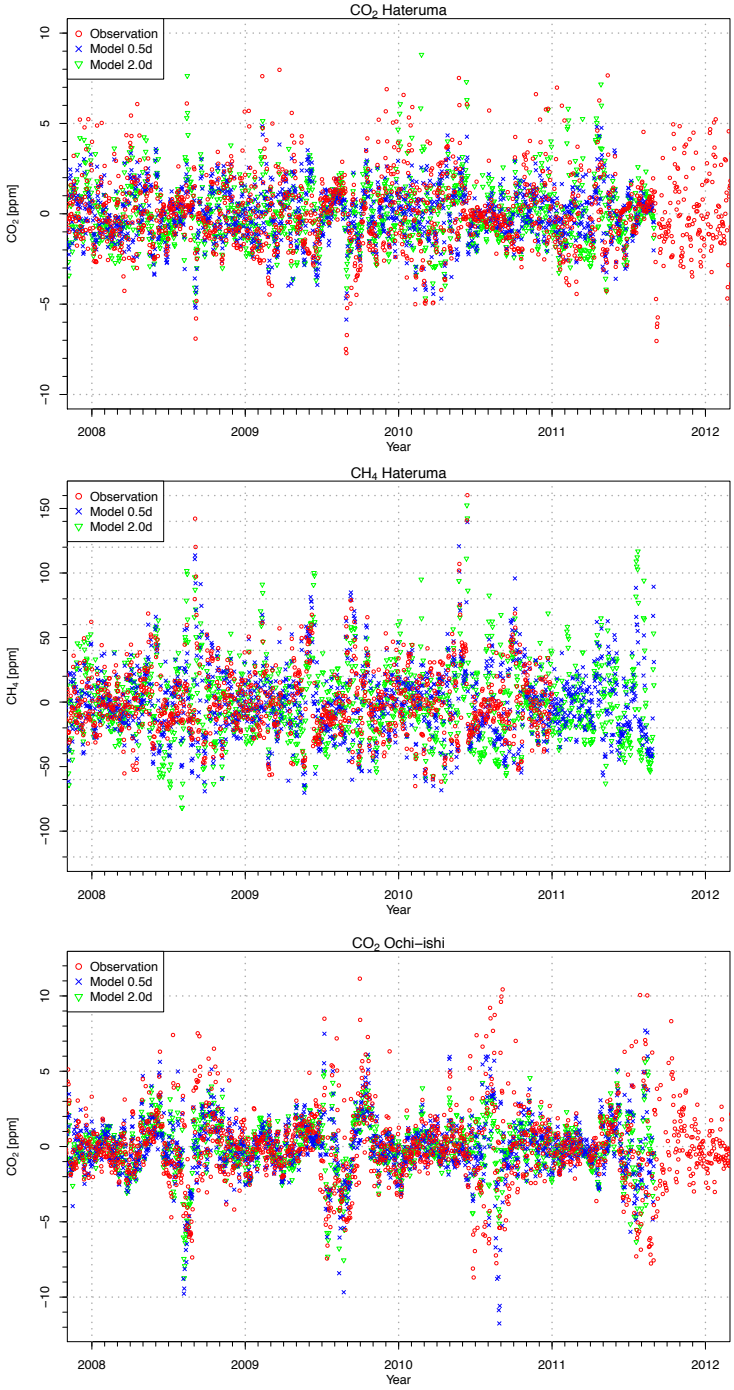

1150

1151 **Fig. 7.** Synoptic variations in observed and simulated time series of daily

1152 mean CO_2 and CH_4 concentrations at Hateruma site and CO_2 concentration at

Ochi-ishi site. “0.5d” and “2.0d” in legends indicate 0.5-degree simulation and 2.0-degree simulation, respectively.

1156

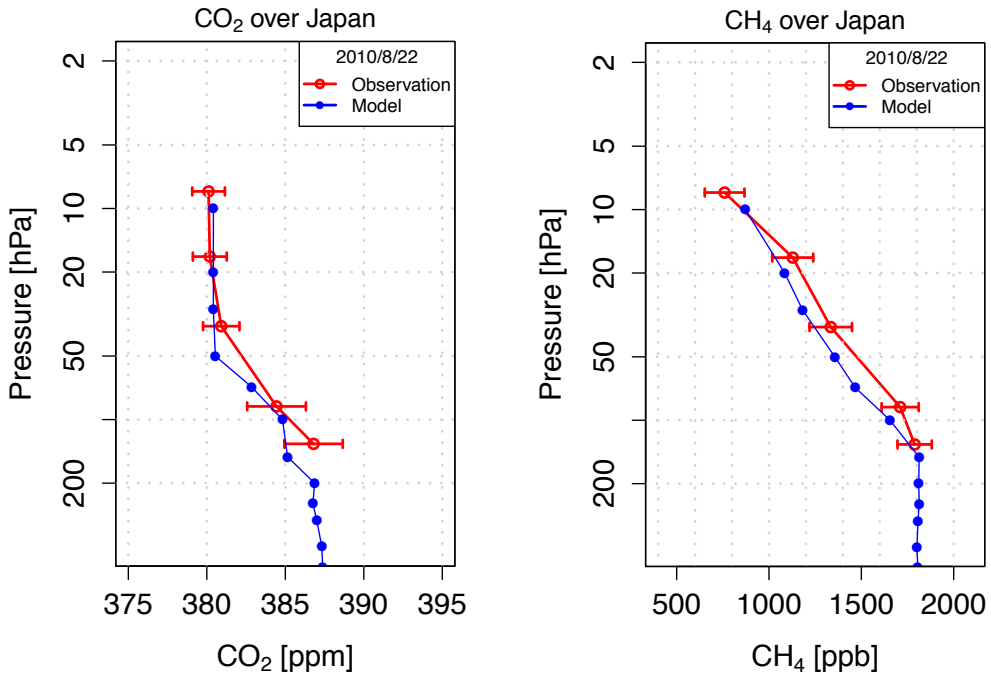

1157

1158 **Fig. 8.** Vertical profiles of CO_2 (left) and CH_4 (right) in the stratosphere over
1159 Japan. The blue lines indicate NIES TM simulated data on 22 August 2010.
1160 The red lines are observed average profiles and their standard deviations de-
1161 rived from balloon-borne measurements over Sanriku, Japan (141.8°E,
1162 39.17°N).

1163

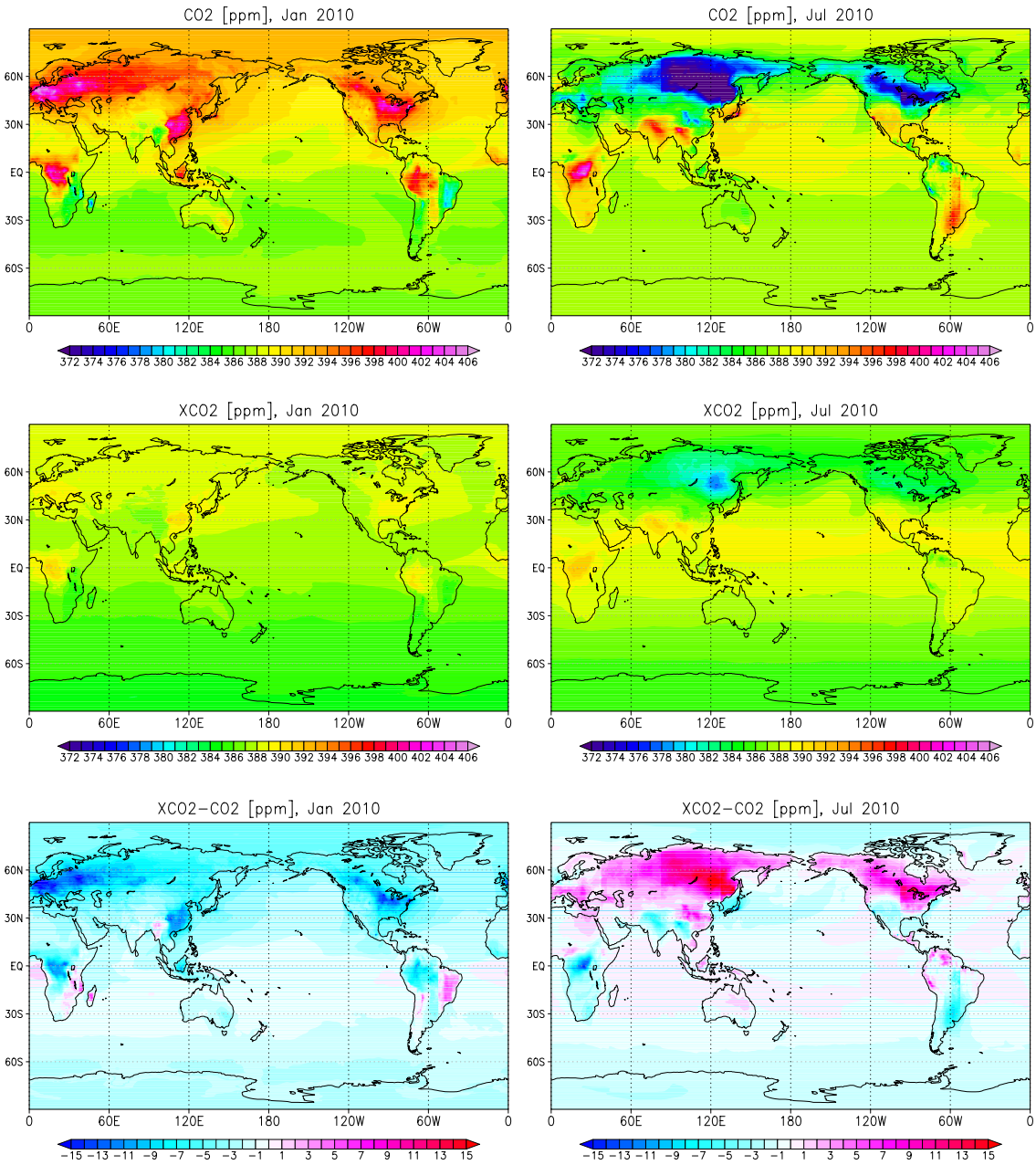

1164

1165 **Fig. 9.** Simulated monthly mean surface CO_2 (top), XCO_2 (middle), and their
1166 differences (bottom) at 13:00 LT in January (left column) and July (right col-
1167 umn) 2010. Ranges of color scales are 372–406 ppm for CO_2 and XCO_2, and –15
1168 to 15 ppm for the differences.

1169

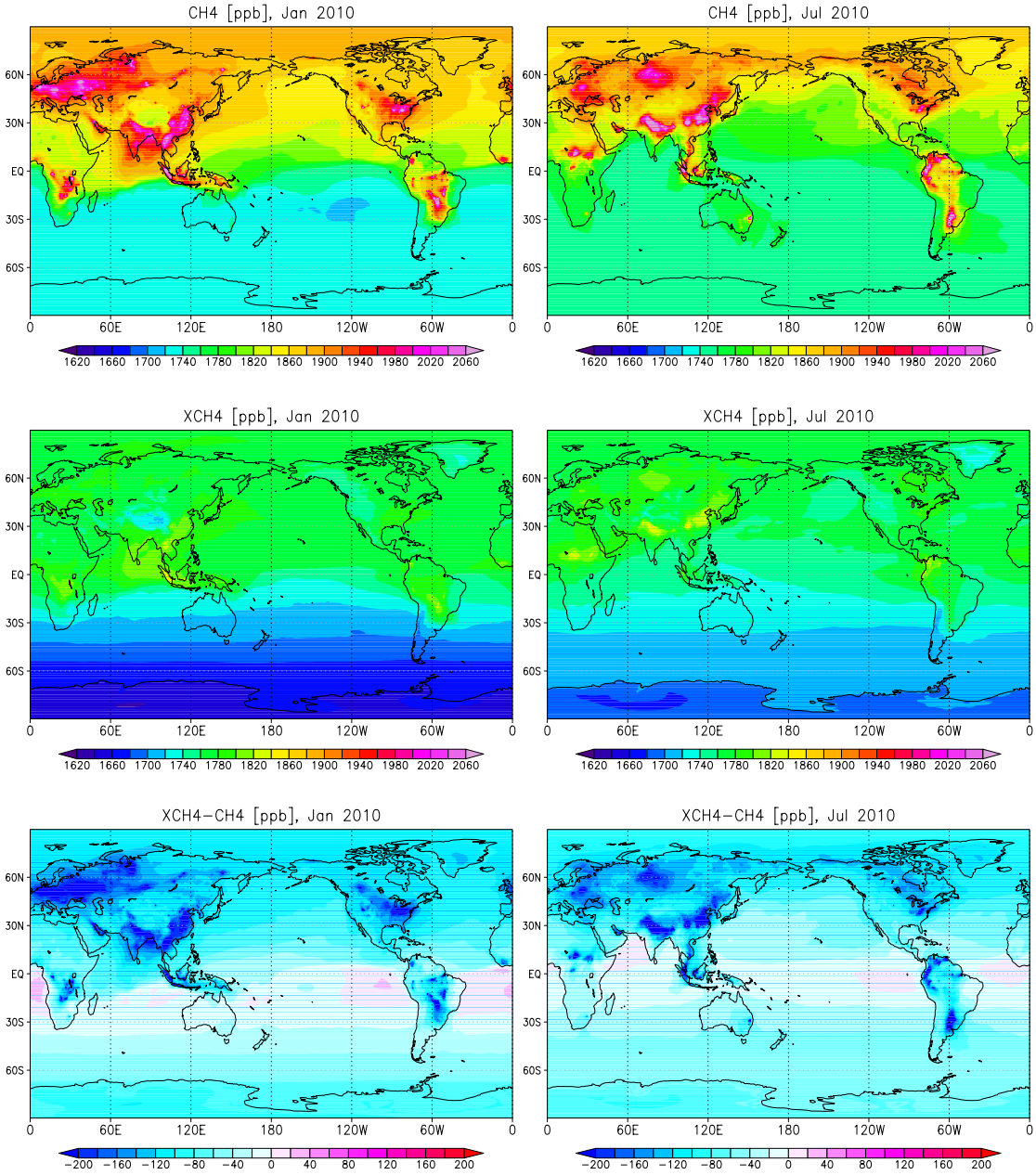

1170

1171 **Fig. 10.** Same as Fig. 7, but for CH_4, XCH_4, and their differences. Ranges of
1172 color scales are 1620–2060 ppb for CH_4 and XCH_4, and –200 to 200 ppb for the
1173 differences.

1174

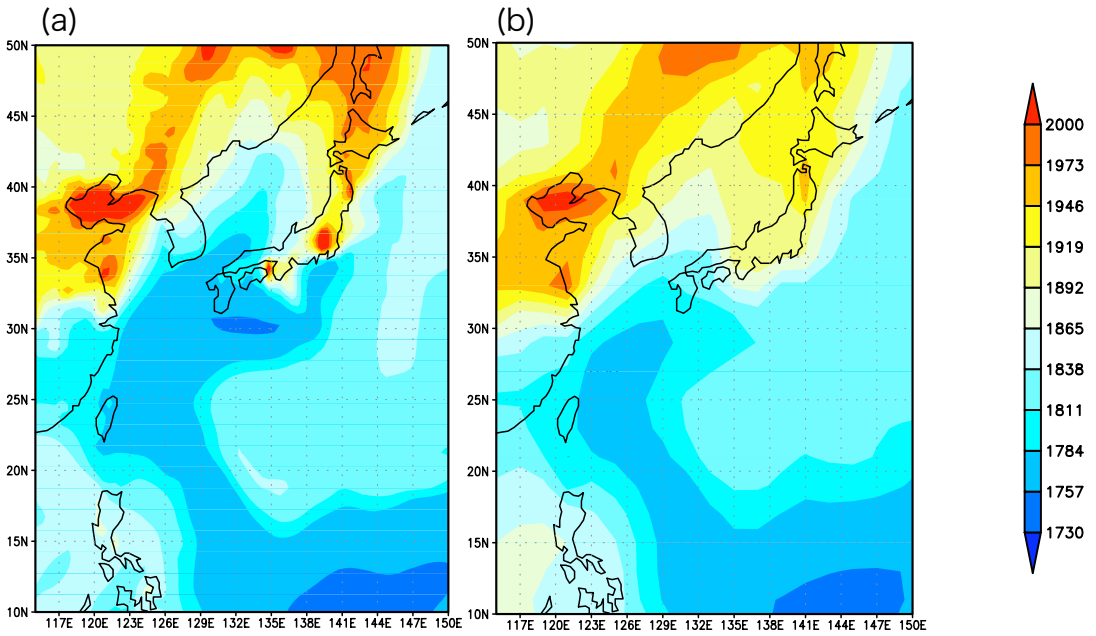

1175

1176 **Fig. 11.** Simulated surface CH_4 concentrations [ppb] around Japan at 13:00
1177 JST on 6 July 2008 with a horizontal resolution of (a) 0.5° and (b) 2.0°.

1178

1179

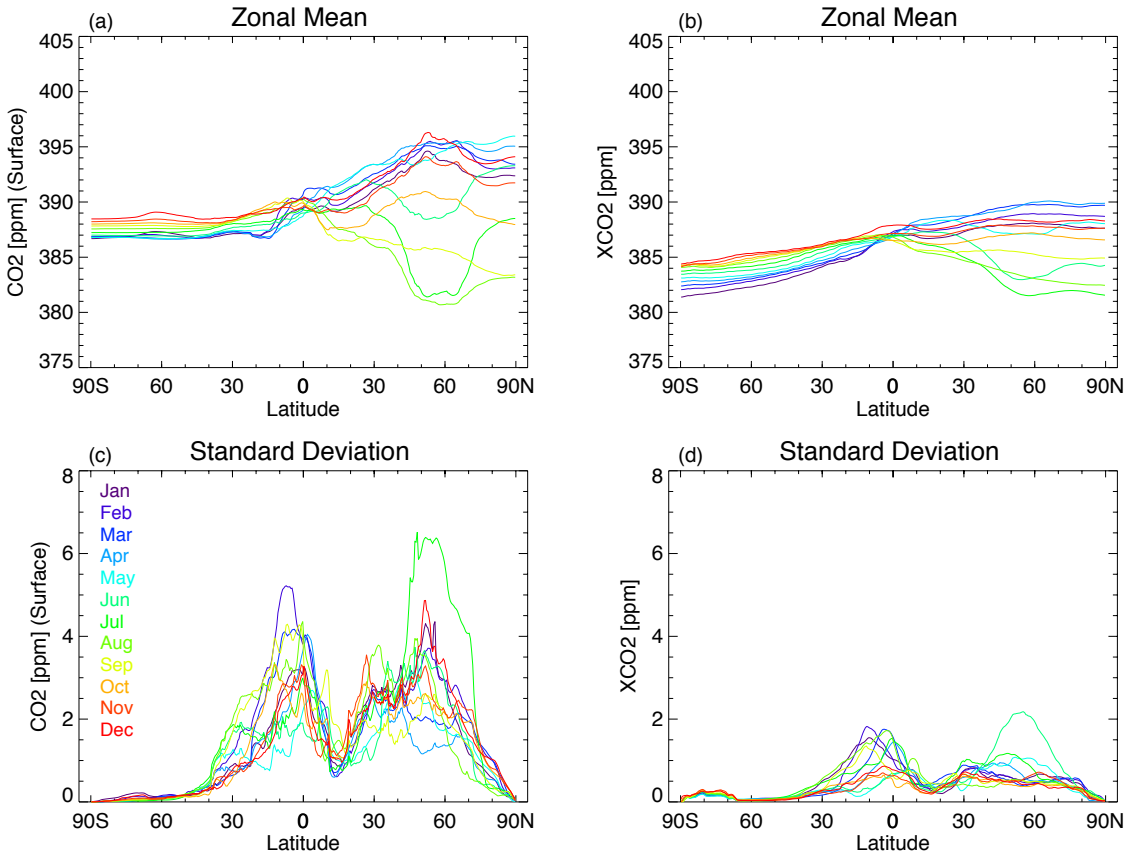

1180

1181 **Fig. 12.** Monthly zonal-mean latitudinal distributions of (a) CO_2 and (b) XCO_2
1182 for 2010 and (c–d) their standard deviations against longitudinal variation.

1183

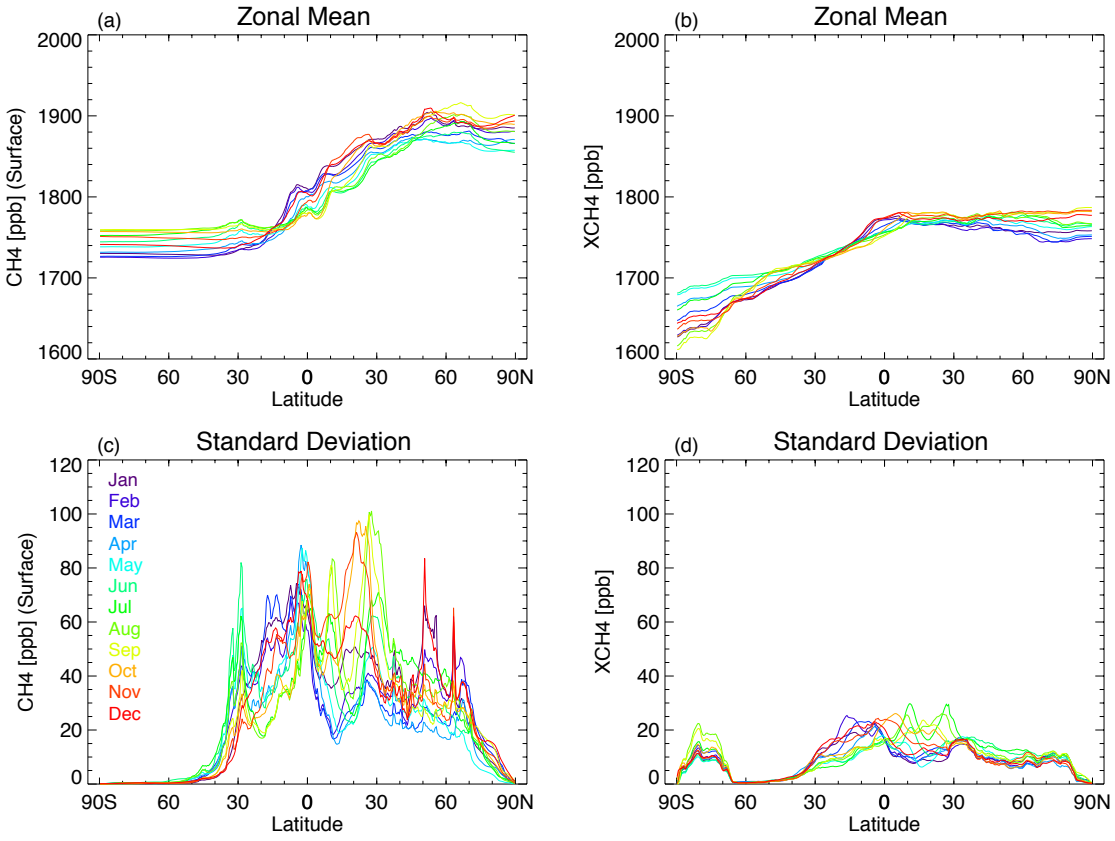

1184

1185 **Fig. 13.** Same as Fig. 11, but for CH_4 and XCH_4.

1186